

CAPACITIVE ARRAY SENSOR FOR TWO-PHASE  
LIQUID CHARACTERIZATION

EILNAZ PASHAPOUR







# Capacitive Array Sensor for Two-Phase Liquid Characterization

by

© Eilnaz Pashapour, B.Sc (Hons)

A thesis submitted to the  
School of Graduate Studies  
in partial fulfillment of the  
requirements for the degree of

Master of Engineering

Faculty of Engineering and Applied Science  
Memorial University of Newfoundland

December, 2007

St. John's

Newfoundland

## Abstract

Two phase or multiphase flows are presented in many process industries such as in our target application, the oil and gas industry. In this thesis, a novel design of a two-phase characterization sensor that measures multiphase flow component fractions is described. Many current sensors are dependent on the flow regime of the multiphase stream; however the proposed method mitigates such dependency by using a phase stratifier. Initially an electromagnetic stratifying was researched however due to unavailability of a strong electromagnetic field needed for a practical system, we used a hydrocyclone stratifier concept afterwards. This device stratifies the flow by different densities of individual phases and is positioned before the entrance of the multiphase flowmeter.

The novel sensor consists of an array of condenser type transducers in a special configuration that uniquely identifies the component fractions under pressure of many disturbances.

A numerical method was conducted using a Finite Element Method (FEM) to simulate the output of the sensor in various flow compositions. Signal processing by Artificial Neural Network (ANN) was adapted and extensively optimized for calculation of the sensor's output.

The proven model and the signal processing method establish a basis for experimental verification that is currently underway.

The work completed to date acts as a starting point from which improvements and extensions can be easily made and incorporated. In this regard, suggestions for future work are presented.

## Acknowledgments

This work has been carried out at the Faculty of Engineering and Applied Science of Memorial University of Newfoundland, Canada. Financial support from the Atlantic Innovation Fund and from the Natural Sciences and Engineering Research Council (NSERC) of Canada is greatly appreciated.

My gratitude goes to my supervisor, Dr. Vlastimil Masek, who suggested my research topic, provided me complete freedom to try ideas and be essentially self-directed. His positive attitude, support, encouragement, and scientific reviewing made me more confident to carry out my research successfully. I am really grateful and admirable to him.

I would like also to thank all the members of the Centre for Instrumentation, Control and Automation (INCA) lab at Memorial University, Farid Arvani, Eranda Harinath, Razzaqul Ahsan and Arpan Karwal for numerous discussions and suggestions at various stages of the work. I also want to thank Richard Newman, Brian Power and the staff for their technical support.

This work would not have been completed without the support of my parents who were always there to support and encourage me throughout my whole life.

At last, but not least, I would like to express my thanks to my fiancé Ashkan Arefi who this work would be impossible without his support and care.



# Contents

1 Introduction.....	13
1.1 Research Objectives.....	15
1.2 Organization of Thesis.....	16
2 Review of Related Work.....	17
2.1 Multiphase Flow .....	18
2.2 Multiphase Flowmeters.....	19
2.2.1 Impedance Technique using Capacitance Sensors .....	20
2.3 Two-Phase (Liquid/Liquid) Separation .....	24
2.3.1 Gravity Separators .....	25
2.3.2 Hydrocyclones .....	26
2.3.3 Magneto-hydro-dynamic Method .....	29
2.4 Concluding Remarks.....	30
3 Impedance-based measuring instrument.....	31
3.1 Stratifying flow .....	32
3.2 Mathematical Model .....	34
4 Stratifying the Flow Using Electromagnetic Separation Method.....	37
4.1 Electromagnetic Principle .....	37
4.1.1 Design of a Magnetic Field Sensor.....	40



4.1.2 DC MODE .....	42
4.1.3 AC MODE .....	43
4.2 Experimental Apparatus for DC Electric and Magnetic Field.....	44
4.3 Experimental Apparatus for AC Electric and Magnetic Field.....	46
4.3.1 Resonance Method.....	47
4.4 Concluding Remarks.....	52
5 Stratifying the Multiphase Flow Using a Hydrocyclone .....	53
5.1 System Configuration .....	55
5.1.1 System Fabrication.....	58
5.2 The Sensor Design .....	62
5.2.1 Design Objectives .....	63
5.2.2 Design Consideration.....	63
5.2.2.1 The geometry and shape of the sensor.....	63
5.2.2.2 Employing the guard electrodes.....	64
5.2.3 Mechanical Dimensions.....	65
6 Numerical Modeling .....	73
6.1 Software Implementation.....	74
6.2 Simulation .....	76
6.2.1 Cylinder model.....	76
6.2.2 Sensor modeling.....	77
6.3 Evaluation for need of FEM .....	79
6.3.1 Model with Guard Electrodes .....	81

6.3.2 Analysis using variable permittivities.....	85
6.3.3 Analysis of the 90% to 100% regimes.....	90
Data Processing using Artificial Neural Network (ANN) .....	92
7.1 ANN Background .....	93
7.2 Implementation and Results.....	96
7.2.1 Data collection .....	96
7.2.2 Pre-processing of data.....	97
7.2.3 Implementation of neural network in MATLAB.....	98
7.2.4 Results and Discussion .....	99
7.3 Concluding Remarks.....	101
8 Conclusion and Future Work.....	106
9 APPENDIX.....	108
10 Bibliography .....	112

# List of Figures

1.1 The diagram for offshore conventional component fraction measurements .....	14
1.2 The diagram for individual well monitoring of multiphase meters .....	15
2.1 Flow regimes for a horizontal pipe .....	18
2.2 Current Multiphase metering system .....	19
2.3 Equivalent capacitance circuits.....	21
2.4 Capacitor configurations .....	22
2.5 Sensor configuration .....	23
2.6 Configuration of the two-coaxial-cylinder capacitor.....	23
2.7 ECT system modules .....	24
2.8 Phase separator tank.....	25
2.9 LLHC Hydrodynamic flow behavior.....	26
2.10 Bradley and Rietema hydrocyclones .....	27
2.11 Geometrical configuration of the hydrocyclone. ....	28
2.12 Colman and Thew hydrocyclone geometry .....	29
2.13 Principle of MHD separation method. ....	30
3.1 Flow regimes in a pipe and the desired stratified flow .....	33
3.2 Schematic of three electrode ring capacitances .....	35
4.1 Direction of electromagnetic force. ....	38



4.2	The Archimedes electromagnetic force acts upward .....	39
4.3	Configuration of the electromagnet, in parallel connection.....	40
4.4	Typical Bipolar Configuration with Low ( $< -500$ ppm) Compensation. ....	41
4.5	Schematic of designed magnetic sensor (AD22151) .....	41
4.6	Calibration and calibration graph of AD22151 magnetic sensor.....	41
4.7	Resulting magnetic field of the electromagnet by varying the distance (d). ....	43
4.8	Configuration of the electromagnet, in parallel connection.....	45
4.9:	Resulting force on each cycle. ....	46
4.10	Impedance of resistance, inductance, and capacitance in series. ....	49
4.11	Configuration to find resonant of the circuit.....	50
4.12	Configuration of the resonant circuit. ....	51
4.13	The experimental view of the AC mode. ....	51
5.1	Schematic view hydrocyclone .....	54
5.2	Schematic view of the fluid flow inside the new hydrocyclone .....	56
5.3	Geometrical configuration of the hydrocyclone .....	57
5.4	Actual configuration of the designed hydrocyclone after fabrication. ....	59
5.5	Flanges that are attached to the system.....	60
5.6	Final Schematic of the Hydrocyclone.....	61
5.7	Cross section of the inner and outer part of the new designed sensor. ....	66
5.8	Schematic of the new designed capacitance sensor .....	67
5.9	2D Plot of Inner and outer layer of the designed sensor.....	68
5.10	New designed sensor with the stands dimensions .....	70

5.11	Designed capacitance sensor.....	71
5.12	Designed capacitance sensor and the hydrocyclone. ....	72
6.1	Finite element for an electrostatic analysis.....	75
6.2	Schematic of the cylinder model in ANSYS. ....	77
6.3	Cross section of one of the capacitances without guard electrodes .....	78
6.4	FEM C1.....	80
6.5	FEM C2.....	80
6.6	FEM C3.....	80
6.7	Schematic and cross section model of $C_2$ with guard electrodes. ....	81
6.8	Approximation using Concentric Cylinders Model .....	82
6.9	Final Schematic.....	85
6.10	$C = C(\alpha_w, \alpha_{oil}, \alpha_w = 75)$ .....	89
6.11	$C = C(\alpha_w, \alpha_{oil}, \alpha_w = 80)$ .....	89
6.12	$C = C(\alpha_w, \alpha_{oil}, \alpha_w = 85)$ .....	89
6.13	Inverse semi-log for $C = C(\alpha_w, \alpha_{oil}, \alpha_w = 75)$ .....	90
6.14	Inverse semi-log $C = C(\alpha_w, \alpha_{oil}, \alpha_w = 80)$ .....	91
6.15	Inverse semi-log for $C = C(\alpha_w, \alpha_{oil}, \alpha_w = 85)$ .....	91
7.1	Nonlinear model of neuron. ....	93
7.2	Sigmoid function for varying slope parameter a .....	94
7.3	Fully connected feedforward network with hidden layer and output layer .....	96
7.4	Schematic of the designed network with two hidden layers.....	99

7.5	Training performance with epochs of 3500 .....	100
7.6	Schematic of the designed network of one layer with 10 neurons. ....	100
8.1	Control Loop: Two-phase Separator and Flow-sensor Evaluator.....	107



# List of Tables

Table 2.1: Geometric property of two well-known families of hydrocyclones .....	27
Table 4.1: Linear values of magnetic field and current for different distances. ....	42
Table 4.2: The linear values of magnetic field and current for d=30mm. ....	44
Table 4.3: Experimental values for resonant. ....	50
Table 6.1: Comparison table of cylinder equation and our sensor. ....	79
Table 6.2: Comparison value of capacitances with and without guard electrode.....	81
Table 6.3: $C1 = C_1(\alpha_w)$ , $\epsilon_{water} = 80$ , $\epsilon_{oil} = 3.0$ .....	83
Table 6.4: $C2 = C2(\alpha_w)$ , $\epsilon_{water} = 80$ , $\epsilon_{oil} = 3.0$ .....	83
Table 6.5: $C3 = C3(\alpha_w)$ , $\epsilon_{water} = 80$ , $\epsilon_{oil} = 3.0$ .....	84
Table 6.6: Final simulated values for Capacitance 1.....	86
Table 6.7: Final simulated values for Capacitance 2.....	87
Table 6.8: Final simulated values for Capacitance 3.....	88
Table 7.1: The final simulated results.....	102

# Chapter 1

## Introduction

Multiphase flows exist widely in process industries. It is important to correctly measure volumetric fractions of such flows in order to automate and optimize these processes. In this thesis an offshore oil and gas production is considered. Figure (1.1) illustrates a conventional offshore measuring setup on a petroleum platform, where a test separator and several single-phase flowmeters are used in the measurement. However, this method requires a large offshore platform space which is costly. Also this method offers only weekly data whereas the production optimization needs real-time measurement. To overcome this problem, a multiphase flowmeter is proposed to measure component fractions at each production well-head in real time. This concept is shown in Figure 1.2 (Field B).

Among various methods available for measuring the component fraction, non-intrusive means are the most desirable. Current industrial applications are using techniques such as  $\gamma$ -ray attenuation, microwave attenuation, pulsed neutron activation (PNA), nuclear

magnetic resonance (NMR) and electrical impedance techniques [9] due to their non-invasive nature. However, the attenuation based flowmeters and the electrical impedance flowmeters are highly flow regime dependent, while the flowmeters based on PNA and NMR are too complicated and extremely costly [9]. The presence of diverse flow regimes and the phase property drifting are the main challenges to be overcome. Analyzing the above techniques; the electrical impedance techniques show advantages such as the low cost, fast dynamic response, and reasonable accuracy. This particular technique is also the most suitable one for the proposed method as it offers a seamless integration with the proposed phase stratifier.

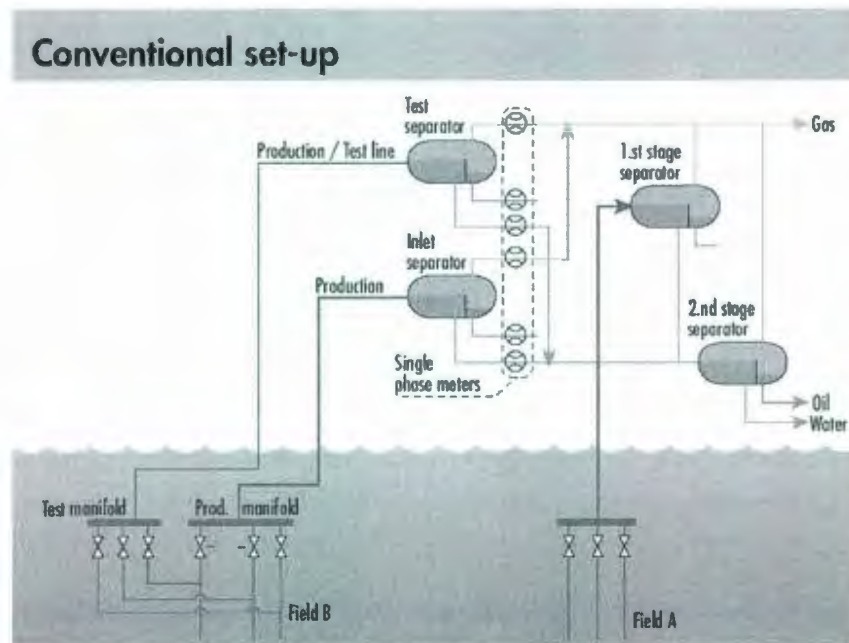


Figure 1.1: The diagram for offshore conventional component fraction measurements [8]



## Individual well monitoring by Multiphase Meters

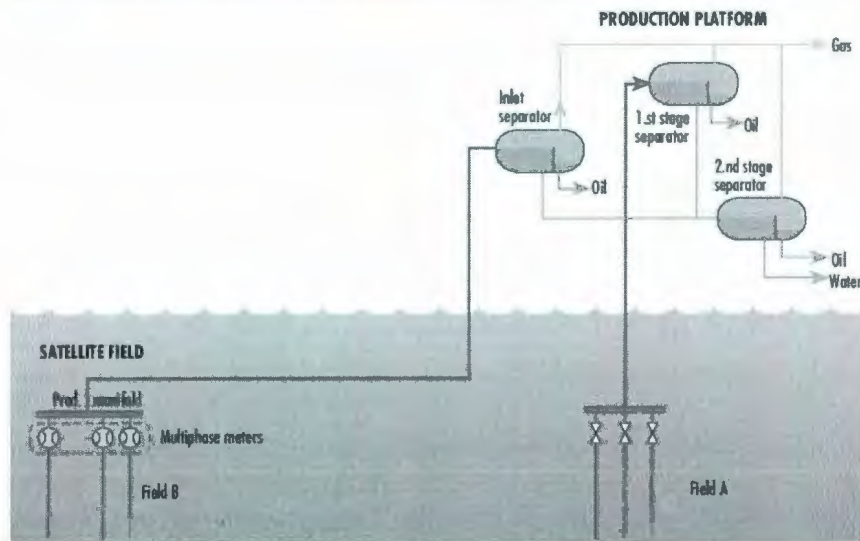


Figure 1.2: The diagram for individual well monitoring of multiphase meters [8].

### 1.1 Research Objectives

The objective of the described research is to develop a low-cost multiphase flowmeter based on a capacitive technique to

- 1- Avoid flow mixing upstream from the measurement ,
- 2- Allow robust subsea installation,
- 3- Be immune to parameter drifting such as due temperature changes, and
- 4- Have accuracy better than 2%.

## 1.2 Organization of Thesis

Chapter 2 gives a discussion on the literature in several related areas. Chapter 3 illustrates the need of having linear independent equations to define the percentage of each flow in crude oil. To stratify the flow, using the electromagnetic method is described in Chapter 4. In chapter 5 the design and implementation of a capacitance-based measuring instrument with a novel hydrocyclone to stratify the flow is explained. Chapter 6 shows the numerical method using FEM to simulate the output of the designed sensor. Data Regression of the simulated data is clarified in Chapter 7. Conclusions and suggestions for future work are presented in Chapter 8.

## Chapter 2

### Review of Related Work

Multiphase flow composition measurement is basically a measurement of volumetric fraction of each phase in the flow. Due to the large diversity of multiphase flows present in process industries the universal flowmeter does not yet exist [6].

The traditional solution of the problem of metering multiphase flow in oil and gas production is to separate the components of the flow first, and then measure the flowrate of each using conventional single-phase instruments. In a typical offshore production platform, a piping manifold isolates flow of crude oil from a production pipeline (riser) into a test separator. The piping manifold plus the testing facility on the platform is very costly, moreover, the measurement is cycled through the entire production field every 3 to 4 weeks depending on the production field size. Multiphase flow meters can on the other hand be installed on every production well head. Moreover, multiphase flow meters can measure the component fractions in real-time [7].



The oil production can thus be significantly improved, however the inherent complexity of crude oil flow and the stochastic changes of flow patterns make the task of designing the meter highly challenging.

## 2.1 Multiphase Flow

The unique feature of a multiphase flow is the presence of diverse flow regimes, the phase distribution in a pipe. In many cases, it is difficult to predict the flow regimes. Normally, the flow structures are affected by the proportions, physical properties and velocity of every component in a crude oil [8]. Process conditions and orientation of the flow play a significant role in determining flow pattern as do the continuous; and dispersed media. Characteristics of the mixture, such as the tendency to form emulsions or foams, the up and down-stream pipework configurations, and the 'history' of the flow also influence the flow pattern at a particular location. Therefore determining the flow regime is a hard task for any designer in the field of multiphase metering. Most flow regimes for horizontal pipes are illustrated in Figure 2.1. In the offshore industry the slug flow is frequently encountered.

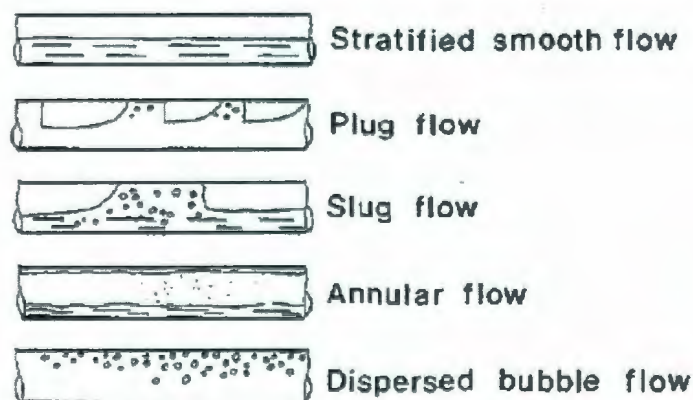


Figure 2.1: Flow regimes for a horizontal pipe [8]

## 2.2 Multiphase Flowmeters

Most of the current multiphase metering systems (MPM) studied in this research employ gamma/X-ray attenuation measurement and statistical methods such as cross-correlation of calculate phase fractions. The meters often use a mixer, which is essential for accurate flow measurement.



Figure 2.2: Current Multiphase metering system [8]

The need for homogenizer/mixer upstream from MPM is a major drawback of the current industrial flowmeters. The tomographical tools such as NMR do not require homogenizer, but are very complex and excessively costly to be widely deployed in large numbers.

In view of these characteristics, this research has been focused on electrical impedance methods.

### 2.2.1 Impedance Technique using Capacitance Sensors

Capacitance sensors have been widely investigated in oil and gas industry: e.g. by Merilo et al (1977), Masuda et al (1980), and Heerens (1986) among others [13, 14] to measure the distance, liquid level measurement, speed and phase percentage of the multiphase pipelines and as its instantaneous output signal has been used to identify the flow pattern, known as tomography. The main principle of capacitance sensors method is based on the relative permittivity of the multi-phases in the flow.

Since the area and distance between the capacitors electrodes are constant, the only contribution to a change is due to a change in the dielectric of the material flowing in between the electrodes.

Two well known methods that have been used in industry which uses capacitance sensors are phase percentage determination and electrical capacitance tomography.

The capacitance method for two-phase flow is based on the differences in the dielectric constants of the oil,  $\epsilon_o \approx 3$  and water  $\epsilon_w \approx 80$ . The capacitance measured across two electrodes is also dependent on the volumetric ratio of the two phases ( $\alpha$ ) which means the resulting output would be in the form of  $C = f(\epsilon_o, \epsilon_w, \alpha)$ . The drawback of the impedance techniques is its sensitivity to the flow regime.



For example Figure 2.3 shows four possible models for four different flow regimes. This may result in sufficiently accurate measurements where the flow regime is time-invariable.

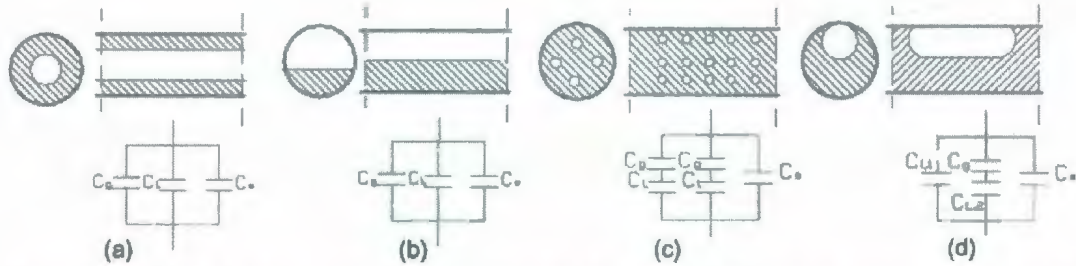


Figure 2.3: Equivalent capacitance circuits for typical flow regimes a) annular flow, b) Stratified flow, c) Bubbly flow and d) Slug flow [13, 15].

A variety of electrode configurations have been also considered by a number of researchers, ranging from flat-plate, concave, helical and multiple wound, where either the electrodes were in contact or isolated from the fluid.

One of the earliest/first researchers [9] examined six different capacitor configurations: a) parallel plates, b) concave plates, c) staggered concave plates, d) double helix, e) multiple helix and f) four concave plates as illustrated in Figure 2.4.

In terms of sensitivity and linearity, the double helix and four concave plates were found to be superior to others. This electrode configuration has been used in many other phase fraction determinations [5, 13, 14] and similar results were obtained. All those sensors were designed with electrodes mounted on the outer surface of the pipe thus isolated from the liquids. Guard electrodes were often installed in to reduce edge effects [14].



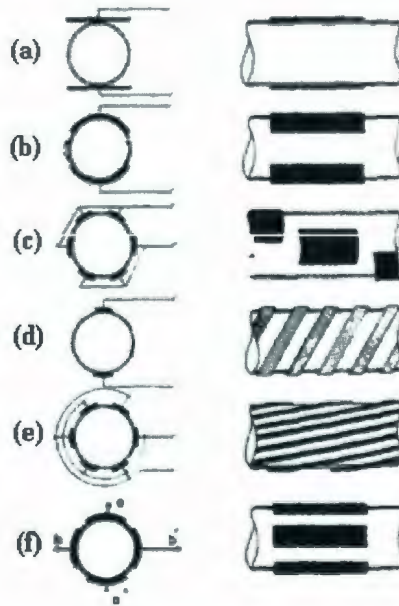


Figure 2.4: Capacitor configurations [9]

Cristina N. Strizzolo and JosC Converti [7] designed a cylindrical sensor with an annular cross section for the fluid passage and the outer electrode, either one of them was isolated (insulated) at a time (Fig. 2.5).

Furthermore a group of researchers designed a coaxial capacitor sensor as illustrated in Fig. 2.6 to determine the phase percentage in multiphase pipelines [16]. The coaxial electrode configuration offers the maximum sensitivity to the measured parameters out of all mentioned configurations and was further developed in this research.

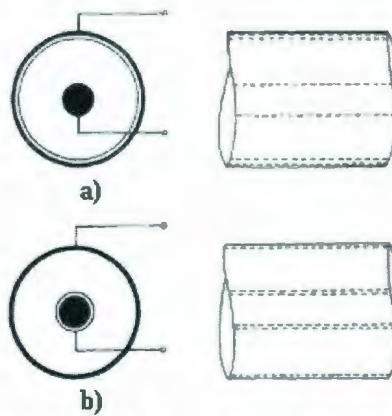


Figure 2.5: Sensor configuration: a) outer and, b) inner electrode isolated [7]

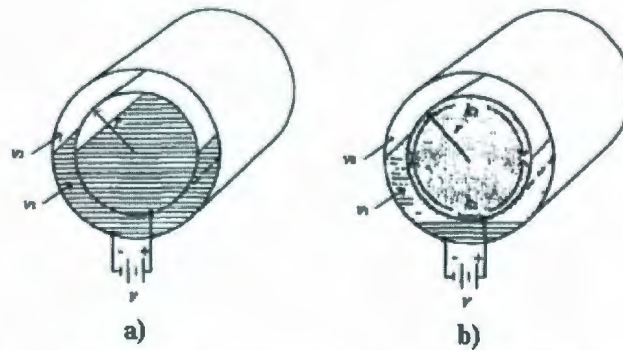


Figure 2-6: Configuration of the two-coaxial-cylinder capacitor a) solid and b) hollow core [8]

Electrical Capacitance Tomography (ECT) is another impedance based techniques that can be to certain extend flow regimes independent [17, 18,19,20]. The fundamental of the ECT technique is by mounting electrodes around the pipe and with measuring [Fig. 2.7] the capacitance of different pairs of electrodes, image reconstruction is possible.

This is a a great advantage over the other techniques, however, due to the large spacing between opposing electrodes and narrow electrode sites, the sensitivities are extremely low, thus less appealing to the industry.

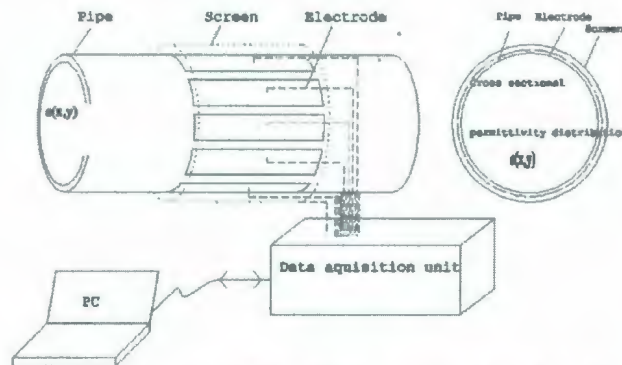


Figure 2-7: ECT system modules. The ECT sensor head with electrodes distributed around the pipe periphery and the data-acquisition unit, which excites the electrodes and measures the interelectrode capacitances, and the personal computer with complementary software installed, for analysis and control [21].

## 2.3 Two-Phase (Liquid/Liquid) Separation

The majority of the electrical impedance techniques to measure the phase fractions are flow regime dependent. Normally, the oil is first separated from water before the measurement is taken; therefore the measurement result no longer depends on flow regime. We are interested in separating phases at the sea bottom level using an inexpensive device compatible with the piping system.

Different techniques of in-line separation are available. The difference in density, conductivity, melting point and others are often used [8]. The next section outlines some of these principles.

### 2.3.1 Gravity Separators

One of the common methods of separating oil from water is to use a gravity technique [22], in which the crude oil is pumped into a tank or series of tanks where oil collects above water and can be skimmed off. The performance of this technique greatly depends on retention time, tank internals and oil properties [22, 27]. To alter the oil properties and improve performance, chemicals, and demulsifying agents are often added. This agent and the heat applied in the tank help to produce the separation of oil and water. As shown in Figure 2.8, after efficient separation time the oil settles on the top of the tank and can be removed from the top section of the tank and from the bottom of the tank the water is skimmed off.

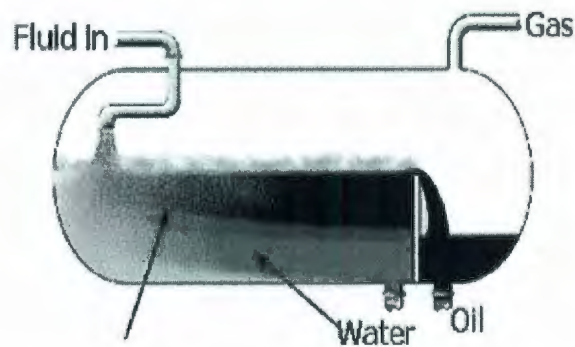


Figure 2.8: Phase separator tank.



### 2.3.2 Hydrocyclones

Hydrocyclones were originally designed to separate solids from liquids [23]. However, in past decades the liquid/liquid hydrocyclones have been widely used by the Petroleum industry.

The first patent of a hydrocyclone is over a century old (Bretnei, 1891), but its first industrial applications date from the late 40's [24].

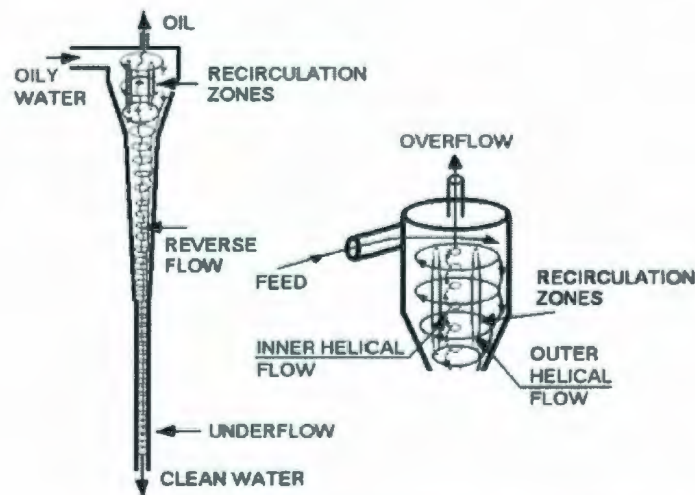


Figure 2.9: LLHC Hydrodynamic flow behavior [25]

The separation of a light dispersed phase (oil) from a heavy continuous phase (water) in a hydrocyclone that is illustrated in Figure 2.9 [25] occurs as a result of a large centrifugal force field caused by the swirling flow. The swirling motion is produced by a tangential injection of pressurized fluid into the hydrocyclone body. The flow pattern consists of a spiral within another spiral moving in the same circular direction. There is a forced vortex in the region close to the hydrocyclone axis and a free-like vortex in the outer

region. The outer vortex moves downward to the underflow outlet, while the inner vortex flows in a reverse direction and goes up in an even stronger vortex motion and out through the overflow pipe, carrying the lighter (oil) particles .

Therefore the two liquids, with different liquid density can separate form each other.

Some well established geometrics of hydrocyclones are overviewed next.

A schematic of an efficient design by Bradley and Rietema (1965, 1961) is illustrated in Figure 2.10 with parameters listed in Table 2.1 [26, 27].

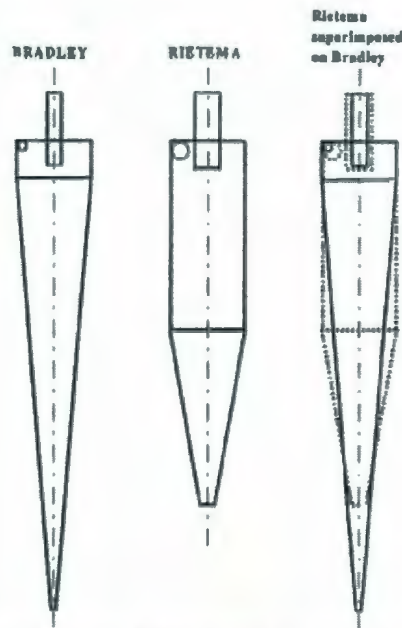


Figure 2.10: Bradley and Rietema hydrocyclones [27].

Hydrocyclone	$D_i/D_c$	$D_o/D_c$	$L/D_c$	$L_1/D_c$	$\ell/D_c$	$\theta$
Bradley	1/7	1/5	-	1/2	1/3	9°
Rietema	0.28	0.34	5	-	0.4	20°

$D_c$ : Hydrocyclone diameter (m)

$D_i$ : Feed inlet diameter (m)

$D_o$ : Overflow diameter (m)

$D_u$ : Underflow diameter (m)

$L$ : Hydrocyclone length (m)

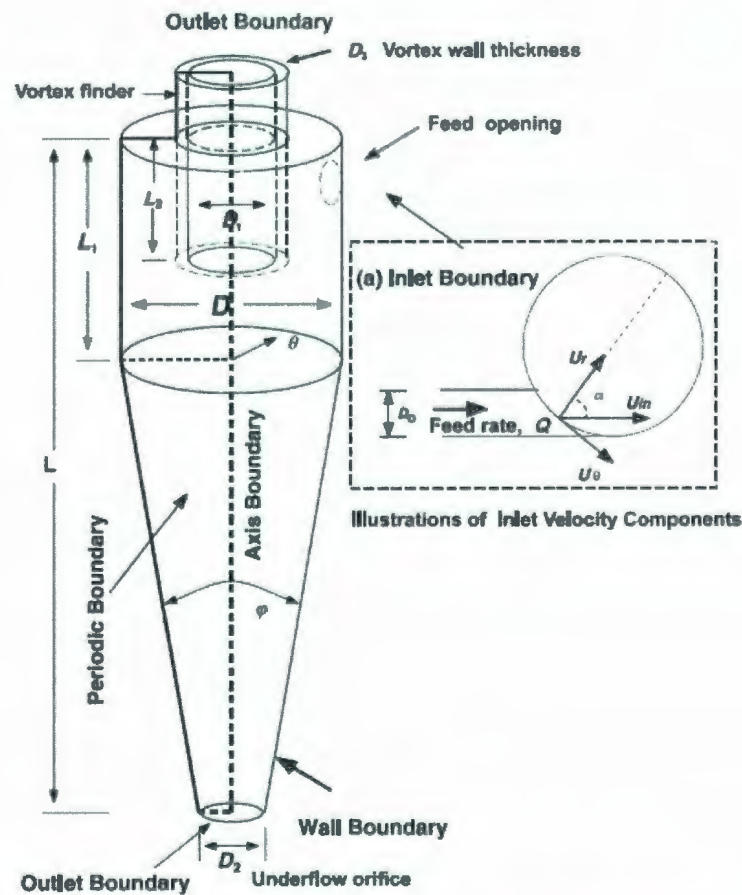
$L_1$ : height of hydrocyclone cylindrical part (m)

$\ell$ : Vortex finder length (m)

$\theta$ : angle of the hydrocyclone cone

Table 2.1: Geometric property of two well-known families of hydrocyclones [24].

Bradley hydrocyclones provide higher efficiencies, while Rietema hydrocyclones give higher capacities. Their designed hydrocyclones is a well-known unit operation, which has numerous applications in separation of biological materials and also in yeast industry. Another recognized method that came in 1983 is the Dabir's experimental model that is shown in Figure 2.11 [29, 30]. This method is very popular in liquid/liquid separations.



D	D0	D1	D2
76mm	0.28D	0.34D	0.16D
D3	L	L1	L2
3mm	5D	0.67D	0.4D

Fig. 2.11: Geometrical configuration of the hydrocyclone [29].



Unlike the other methods designed by, Colman and Thew (1988) has four cylindrical and conical sections [22, 28], as shown in Figure 2.12. Inlet and the reducing section are designed to achieve higher tangential acceleration of the fluid. Colman and Thew proved that their longer double-cone hydrocyclone could separate oil-water mixtures [31, 35].

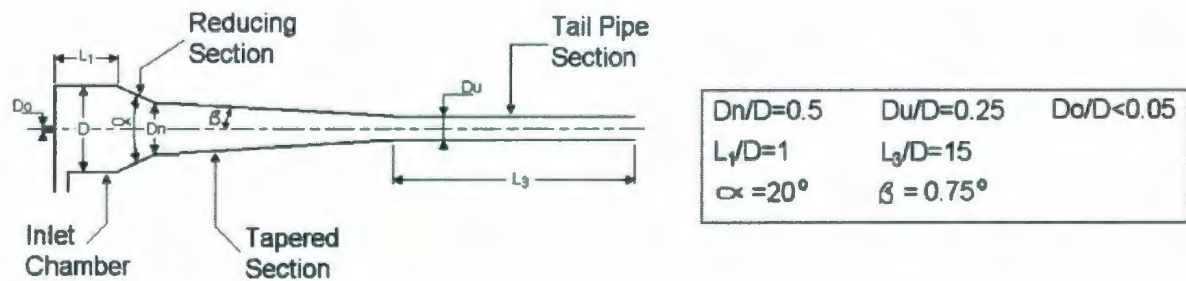


Figure 2.12: Colman and Thew hydrocyclone geometry [25]

### 2.3.3 Magneto-hydro-dynamic Method

A conceptually different method for oil/water separation is using an electromagnetic force (magnetohydrodynamics force). Fig 2.13 shows the principle of the MHD method. A magnetic field is applied in the direction of water flow and electric current is applied perpendicular to the magnetic field using electrodes. Then, the water is subject to electromagnetic force, according to Fleming's rule [34]. This induced force together with the gravity field increases the buoyancy effect on the oily particles. This method has been studied as described in chapter 4. There is however disadvantages associated with this



method, when it comes to industrial applications dealing with oil/gas streams. First, the method requires strong magnetic fields generated by superconducting magnets, secondly, the electric current in the conductive phase, here water, poses a security hazard in the presence of flammable liquids and gases.

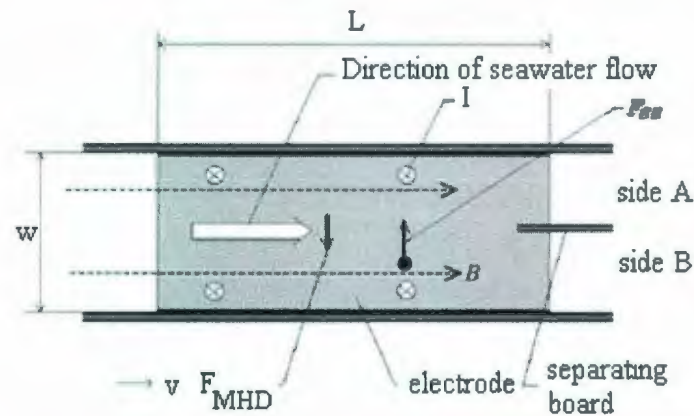


Figure 2.13: Principle of MHD separation method.

## 2.4 Concluding Remarks

This chapter gives a background of the multiphase flow metering technologies, and different separation methods for stratifying the flow. In the following chapters, design of the meter and stratifier is described.

## Chapter 3

### Impedance-based measuring instrument

A capacitance type or impedance-based multiphase flow meter is employed to measure the component fraction in this research.

The electrical impedance (capacitance) is measured across two electrodes, between which an oil/water mixture is flowing. The impedance is dependent on the geometry and construction of the sensor, the dielectric properties of the individual fluids, the flow regime and the components fraction  $\alpha$  (or volumetric ratio) of the flow. However, if the first three factors are constant then the measured impedance will be a direct function of the component ratio (volumetric fraction).

We have developed a phase stratifier that converts variable flow regimes into a stratified flow where possible.<sup>1</sup> In the real process water permittivity can vary in the range of  $\epsilon_{water} = 75 \sim 85$  and oil permittivity  $\epsilon_{oil} = 2.5 \sim 3.5$  [4] mainly due to different chemical contents and temperature drifting. These factors are not constant; therefore the capacitance will be a function of three variables of

---

<sup>1</sup> Emulsion can not be separated easily

$$C = f(\alpha, \epsilon_{\text{water}}, \epsilon_{\text{oil}}) \quad (3.1)$$

where  $\epsilon_{\text{water}}$  is the relative permittivity of water,  $\epsilon_{\text{oil}}$  is the relative permittivity of oil and  $\alpha$  is the volumetric fraction of oil in water.

The objective is to design a measurement independent of  $\epsilon_{\text{water}}$  and  $\epsilon_{\text{oil}}$ .

### 3.1 Stratifying flow

The majority of electrical impedance techniques to measure the component fractions in process are flow regimes dependent [36]. Different type of flow regimes are shown in Figure 3.1. Multiphase flow meters have attempted to address the problem of measurement across such a wide range of conditions in two different ways before the fluid enters the measurement sensor:

1. Mix the fluid (Homogenous)
2. Stratify the fluid

The first method is to condition the flow to suit the measurement principle in use, usually by attempting to generate a uniform spatial distribution of the oil/water mixture over a given cross-section. This method pre-mixes the flow to attempt and ensure that all measurements are made with a homogenous flow, thus removing the problem of flow regime dependency.

Method 2 stratifies the flow regimes so the phases are separated as shown in Figure 3.1.

This method is chose for our research.

To overcome the impedance sensor's dependency on the flow regime in Method 2, two methods are proposed to form a stratify flow in the front of the impedance sensor.

- a. Stratifying flow using electromagnetic separation method
- b. Stratifying flow using Hydrocyclone device

Method "a" uses the concept of electromagnetic separation method for separating flow, oil from water, because water conducts electricity, it can be subjected to a Lorentz force.

Method "b" proposes a novel hydrocyclone device which can rotate the multiphase flow and form stratified flow in terms of the different densities of the oil/water in crude oil.

This method uses the concept of centrifugal force to stratifying the flow.

Both of the methods and their process will be discussed in the following chapters for stratifying the flow.

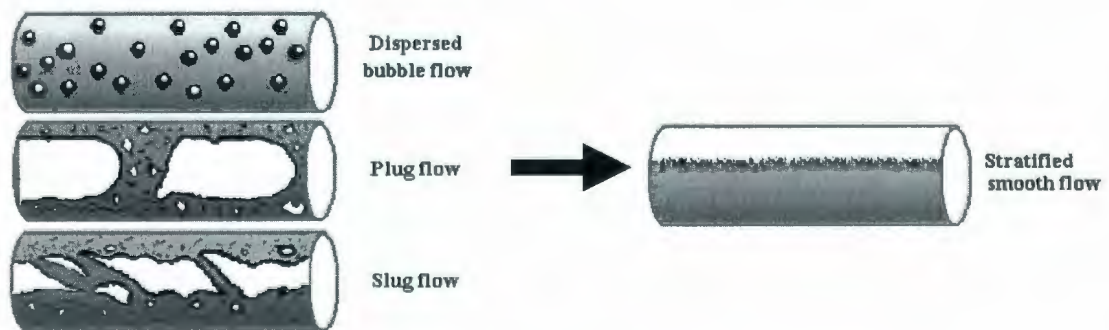


Figure 3.1: Flow regimes in a pipe and the desired stratified flow



## 3.2 Mathematical Model

The fraction of oil and water flowing between two insulated electrodes is determined by measuring the capacitance across the sensor. With three unknowns of  $\epsilon_{water}$ ,  $\epsilon_{oil}$  and  $\alpha$ , there is a need for three linearly independent equations that

$$C_1 \neq \alpha C_2 \neq \beta C_3 \quad (3.2)$$

where  $C$  [Farads] is the resultant measuring capacitance across the sensor.

The resulting capacitances of parallel plates have a linear dependent [37] equation which is not helpful for solving our equation (3.1).

A three ring electrode sensor is proposed to provide three linearly independent equations [Figure 3.2]. The configuration is set to have an inner electrode ring and an outer electrode ring with a stratified multiphase flow confined between the electrodes.

The heights ( $H$ ) of the electrodes are considered constant with inner radiuses of  $r_1, r_2, r_3$  and outer radiuses of  $R_1, R_2, R_3$ . The sensor's configuration be designed to stratify water near the outer electrode and oil near the inner electrode; subsequently  $\zeta_1, \zeta_2, \zeta_3$  are the boundaries of water and oil.

The three measuring capacitances for the three sets of electrodes are derived in equations (Eq 3.3), (Eq 3.4) and (Eq 3.5). The three derived equations are linearly independent of each other. Each equation is a function of the component fraction plus the material constant, the relative permittivity which is considered to be confined in these ranges:

$$\epsilon_{water} = 75 - 85 \text{ and } \epsilon_{oil} = 2.5 - 3.5.$$


$$C = \frac{C_{\text{water}} \times C_{\text{oil}}}{C_{\text{water}} + C_{\text{oil}}}$$

$$\text{where: } C_{\text{water}} = \frac{\ln(R_1 / \zeta_1)}{2\pi\epsilon_0\epsilon_{\text{water}}H}$$

$$C_{oil} = \frac{\ln(\zeta_1 / r_1)}{2\pi\epsilon_o\epsilon_{oil}H}$$

Which forms the formula for individual electric pair capacitances as:

$$C1_{total} = \frac{2\pi\epsilon_o\epsilon_{oil}\epsilon_{water}H}{(\epsilon_{water} - \epsilon_{oil})\ln(R_1 - r_1) - \epsilon_{water}\ln(r_1) + \epsilon_{oil}\ln(R_1)} \quad (3.3)$$

$$C2_{total} = \frac{2\pi\epsilon_o\epsilon_{oil}\epsilon_{water}H}{(\epsilon_{water} - \epsilon_{oil})\ln(R_2 - r_2) - \epsilon_{water}\ln(r_2) + \epsilon_{oil}\ln(R_2)} \quad (3.4)$$

$$C3_{total} = \frac{2\pi\epsilon_o\epsilon_{oil}\epsilon_{water}H}{(\epsilon_{water} - \epsilon_{oil})\ln(R_3 - r_3) - \epsilon_{water}\ln(r_3) + \epsilon_{oil}\ln(R_3)} \quad (3.5)$$

The design of the proposed capacitance based multiphase flow meter relies on the process of stratifying the flow before and within the multiphase flow meter. The stratified flow confines oil (lower density) near the inner electrode and water (higher density) near the outer electrode.

This process combined with the novel electrode array configuration results in linearly independent equations for solving the component fraction under variations of electrical permittivities of individual components.

Two methods of stratifying the flow is discussed in the following chapters.

## Chapter 4

### Stratifying the Flow Using Electromagnetic Separation Method

This chapter discusses the issues and challenges uncouned in using electromagnetic method to separate oil from water. Electromagnetic separation method uses Lorentz force to boost the buoyancy effect on the oily phase in water. This method was conducted only a low magnitude of the force was generated.

#### 4.1 Electromagnetic Principle

Fluid phase being electrically conductive such as water of conductivity  $\sigma = 4 - 5 [\Omega^{-1}m^{-1}]$  can be subjected to an electromagnetic force that Lorenz force that can help to separate oil from water using a gravity/buoyancy.

Lorentz Force ( $F$ ) results from the vector product of a current density  $j$  and the magnetic field  $B$

$$F = j \times B \quad (4.1)$$

The current density is given by ohm's law [38]:



$$j = \sigma(E + u \times B) \quad (4.2)$$

Where  $E$  denotes the electric field,  $u$  the fluid's velocity, and  $\sigma$  the electrical conductivity, respectively. Because electrolytes have small conductivities, the induced current ( $u \times B$ ) in Eq. 4.2 is very low. To obtain large current density induced in the flow control it is necessary to apply electric field of magnitude  $E$  and also an independent magnetic field of  $B$  [38]. Lorentz force can be generated by an electromagnet and two electrodes. The magnetic field  $B$  is defined in terms of a force on moving charge in the Lorentz force law [39].

The electric field is defined as the electric force per unit charge. The direction of the field is taken to be the direction of the force it would apply on a positive test charge. The electric field is toward outward from a positive charge and in toward a negative point charge [39]. Using the Fleming's left hand rule (Figure 4.1) the force direction is determined from the direction of electric and magnetic fields.

An externally applied electromagnetic (Lorentz) force, generated by a magnetic field  $B$  and the electric current ( $i$ ), subjects the aqueous phase to separate from oil.

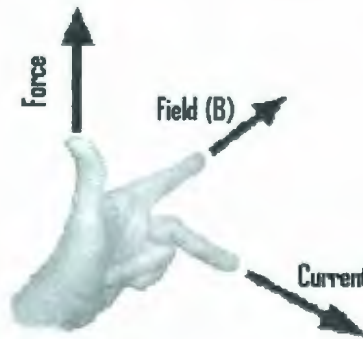


Figure 4.1: Direction of electromagnetic force.

This force will not act on non-conducting substances, oil, since no current can propagate through this phase. As a reaction to this force (Newton's third law), droplets of oil are equally forced in the opposite direction, this force is known as the Archimedes electromagnetic force ( $F_N$ ) as illustrated in Figure 4.2.

$$F_N = -F = -ilB \quad (4.3)$$

To generate a magnetic field we first examined an electromagnet that was part of a magnetic flow meter; however the field was very low; by applying 120V AC, the resultant magnetic field was 0.018 T. Subsequently an electromagnet provided by Memorial's Earth Science Department, was used in the experiment.

The electromagnet of the "C" core of variable gap had two windings that were connected in series and in parallel (Figure 4.3). The parallel connection was chosen to provide stronger fields. Because of non-availability of the magnetic field measurements in the laboratory, a magnetic field sensor is designed and fabricated as outlined next.

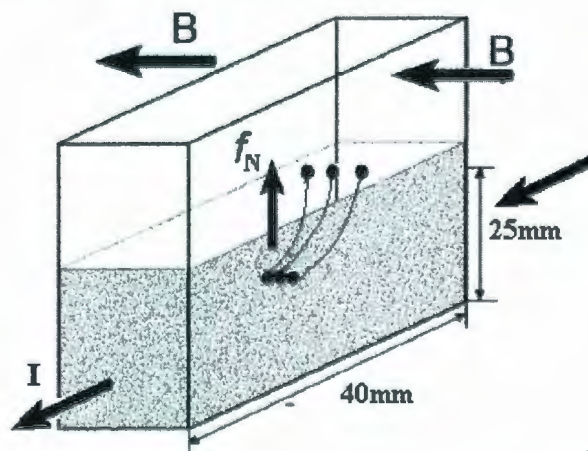


Figure 4.2: The Archimedes electromagnetic force acts upward

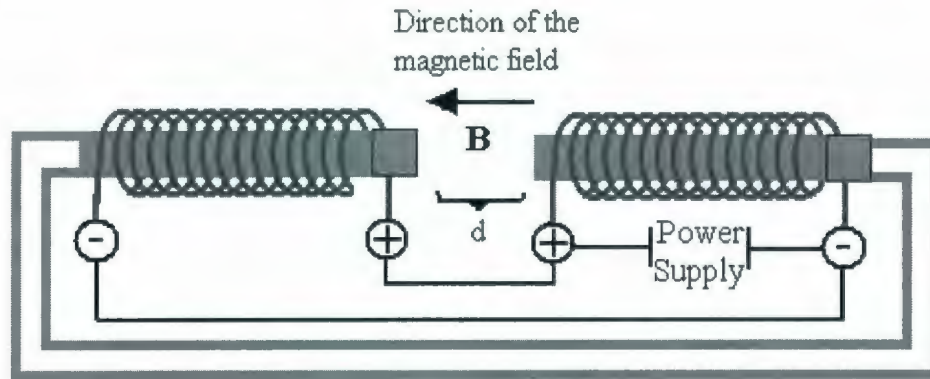


Figure 4.3: Configuration of the electromagnet, in parallel connection

### 4.1.1 Design of a Magnetic Field Sensor

Magnetic field sensor was build using AD22151 (Analog Device) [40]. This Hall sensor is a linear magnetic field transducer. The output of it is a voltage proportional to a magnetic field applied perpendicularly to the top surface of the IC. As shown in the Figure 4.4, a bipolar configuration is chosen because of the usage for both DC (Direct Current) and AC (Alternative Current) modes.

The configuration and component selection for R1, R2 and R3 were chosen according to the data sheet. The sensor requires external component selection for temperature component (R1) and signal gain (R2 and R3). For R1 the potentiometer resistance ranging 1~100K ohms is placed, where in calibration test the range is found to be 20K  $\Omega$  . Also R2 and R3 were chosen to be 1K  $\Omega$  each that results a gain of 1.4 from sensor specification of (Equation 4.4)

$$Gain = 1 + \frac{R3}{R2} \times 0.4mV / G \quad (4.4)$$



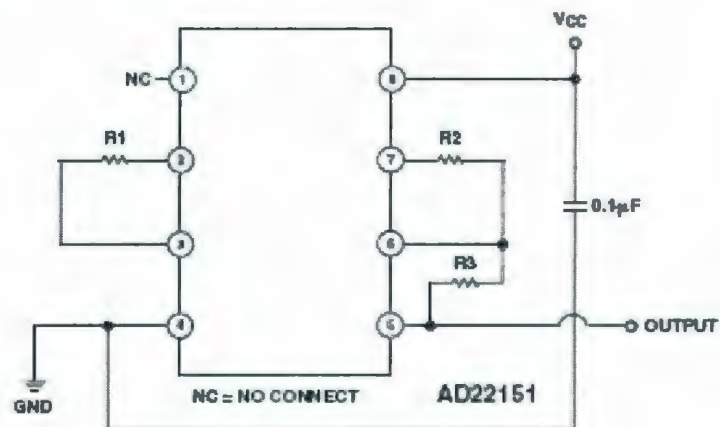


Figure 4.4: Typical Bipolar Configuration with Low ( $< -500$  ppm) Compensation.

Special care was taken when a PCB was designed with the resistances and one capacitance placed far away from the sensor (Figure 4.5).

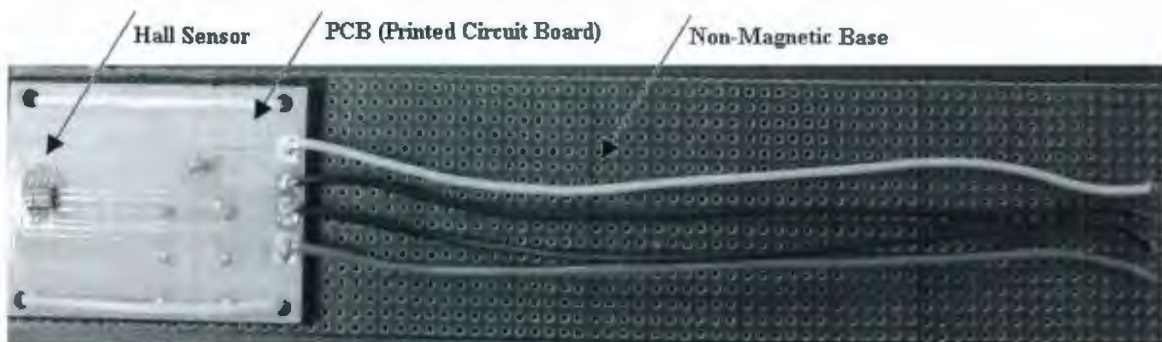


Figure 4.5: Schematic of designed magnetic sensor (AD22151)

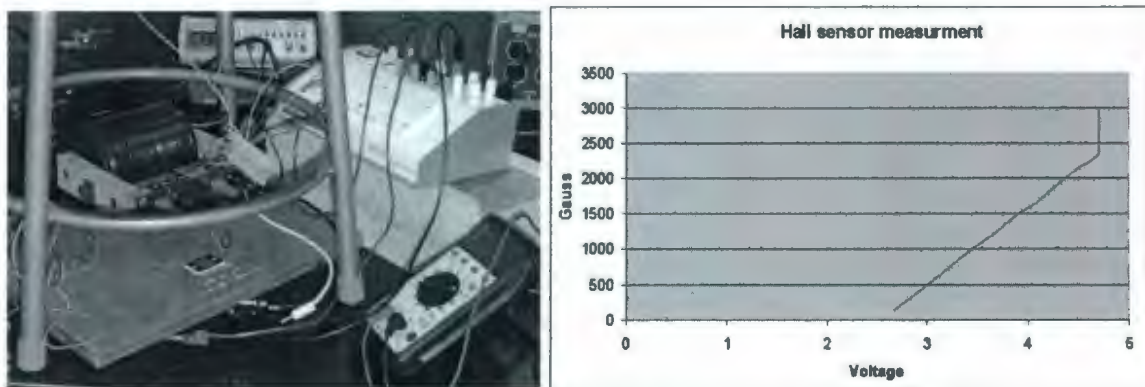


Figure 4.6: Schematic of calibration and calibration graph of AD22151 magnetic sensor.



The calibration graph is plotted as in Figure 4.6. As can be observed from the graph, the linear range of the output is on 0.23T (2300 Gauss).

### 4.1.2 DC MODE

Experiment voltage of 19.6V and current of 3A supplied to the electromagnet resulted in magnetic field of 1800 Gauss (0.18T). The magnitude of the field varies linearly by reducing the current as shown in Table 4.1 and Figure 4.7.

The value of  $d$ , the gap width, has a significant effect on the magnitude of the magnetic field. The smaller gap, the stronger field is obtained. The Dc mode of operation as explained later requires rapid flows to diminish the effect of electrolysis. In order to conduct experiments on static fluids, an AC mode was investigated.

DC Current(A)	DC Voltage(V)	Magnetic field(T) for d=30mm	Magnetic field(T) for d=22mm
0.5	3.3	0.039	0.048
0.75	4.8	0.051	0.0645
1	6.5	0.069	0.087
1.25	8.1	0.084	0.105
1.5	10.1	0.102	0.1305
1.75	11.4	0.111	0.144
2	13.1	0.1245	0.165
2.25	14.8	0.141	0.18
2.5	16.3	0.153	0.198
2.75	18	0.168	0.216
3	19.6	0.18	0.24

Table 4.1: Linear values of magnetic field and current for different distances.

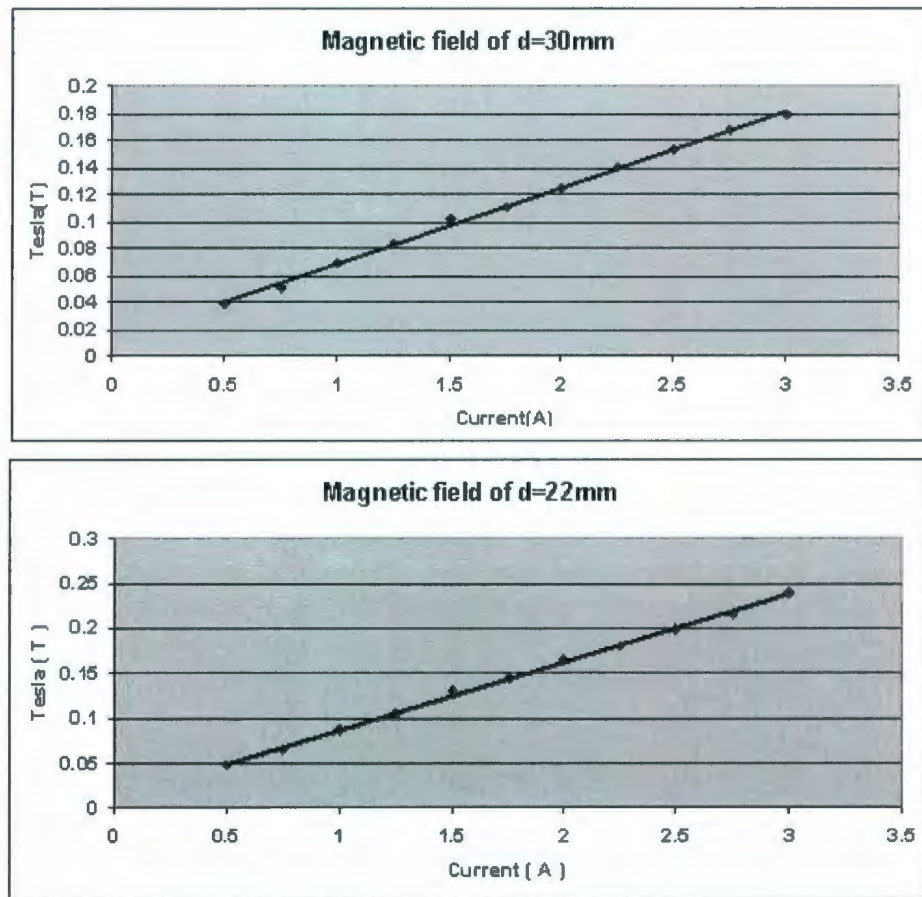


Figure 4.7: Resulting magnetic field of the electromagnet by varying the distance (d).

### 4.1.3 AC MODE

The same procedure was followed for the AC MODE and the resulting magnetic field is plotted in the Table 4.2. The field for both AC and DC modes was measured in the middle of distance between poles.

AC Current(mA)	AC Voltage(V)	Magnetic field(T) for d=30mm
20	66	0.0006
40	124	0.0012
60	165	0.0020
80	207	0.0025
100	242	0.0035
140	317	0.0050
180	391	0.0065
200	432	0.0070
210	459	0.0072
230	497	0.0075
239	518	0.0078

Table 4.2: The linear values of magnetic field and current for d=30mm.

## 4.2 Experimental Apparatus for DC Electric and Magnetic Field

To generate electric field, in these experiments we have selected two  $20 \times 50$  mm rectangular electrodes spaced by 22mm. The electrodes were made of stainless steel and were chosen to be meshed type electrodes to make the conductivity higher thus allowing more current passes through the liquid.

The experimental apparatus for DC experiment consists of a flexible hose 20mm diameter, electromagnet magnetic field, two  $20 \times 50$ mm rectangular meshed stainless steel electrodes to produce the electric field, a DC motor mixer, thermometer to monitor the temperature to stay at around  $25^{\circ}\text{C}$ , and a flow loop as shown in Figure 4.9. The flow experiment was carried out using NaCl aqueous solution with granulated cork particles for better visualization (density of  $0.4 \text{ g/cm}^3$ ), flow ratio of 7 cm/s, magnetic field of



2600 Gauss (0.26T) and electric current of 1.25A. The direction of DC force is determined from the Fleming's left hand rule (Motor Rule) on a current carrying conductor in a magnetic field where the acting force is perpendicular to the electric and magnetic field [38] in the direction of gravity. This results in magnitude of

$$F = qE + ilB = 1.12 \times 10^{-6} + 0.013 \approx 0.013N$$

When using the DC mode, hydrogen and chlorine/oxygen gases were produced at the cathode and anode, respectively, as a result of electrolysis.

To eliminate the effect of electrolysis, we need to either increase the fluid flow dramatically or switch to the AC mode.

The developed gases, namely the hydrogen, also pose a hazard in the presence of large electric fields. This is a very serious issue that makes the DC mode inapplicable in the oil & gas industry. Hence we switched to AC Mode, despite of many successful DC mode applications reported in the literature [41, 42, 43, 47].

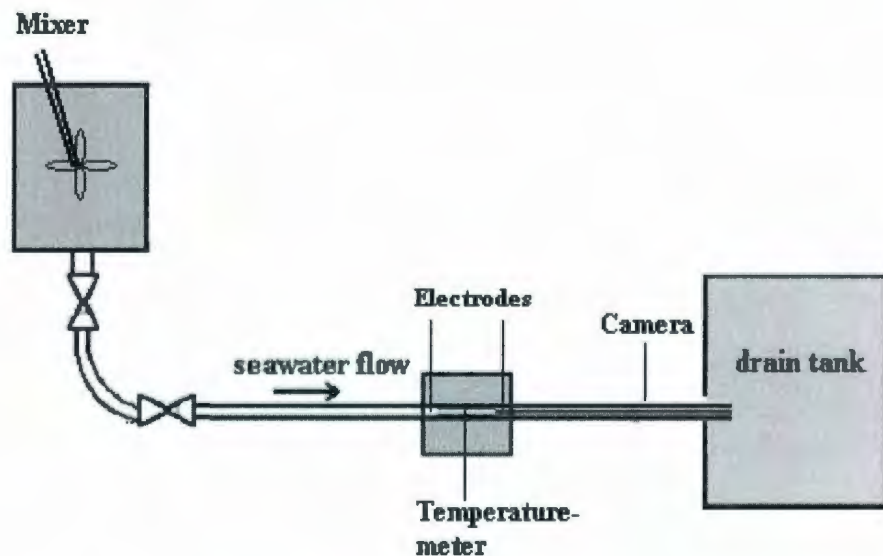


Figure 4.8: Configuration of the electromagnet, in parallel connection



### 4.3 Experimental Apparatus for AC Electric and Magnetic Field

Figure 4.10 shows a schematic diagram of the AC mode experiment consisting of a plexi-glass chamber, an AC electromagnet with magnets 30mm apart, two  $20 \times 50$  mm rectangular meshed stainless steel electrodes 20mm apart, a DC motor-mixer, and the thermometer. The schematic of the circuit is shown in Figures 4.9.

It is important to synchronize the magnetic field with the electric field so that the resulting force assists the separation process. Therefore because both magnetic and electric field are in phase, the resulting force is  $(F = (-i)(l)(-B) = +ilB)$  thus positive and in gravity direction as we desire. As a result the Archimedes electromagnetic force would be in the opposite direction (upwards).

In order to observe the effect of separation using the electromagnetic principle but without other effects such as temperature (since temperature can affect on separation) or hydrolysis, we have limited the current  $i$  to 0.5A.

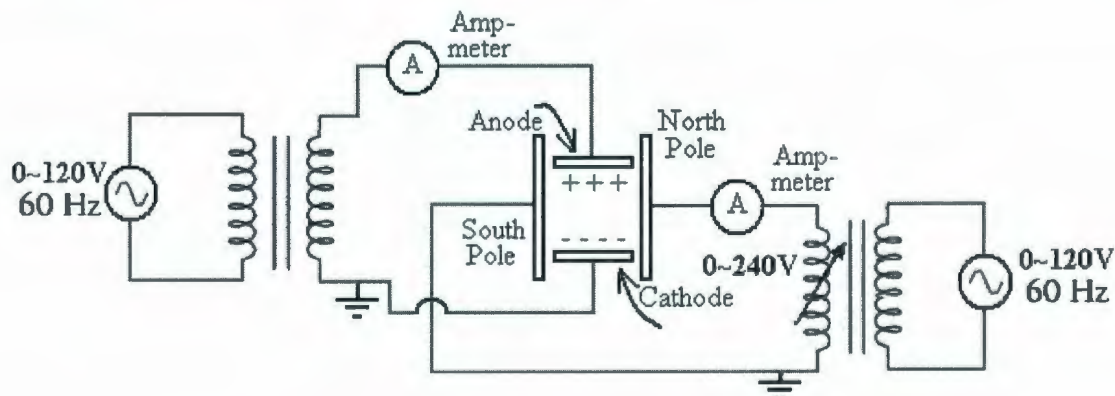


Figure 4.9: Resulting force on each cycle.

The highest magnetic field using a 240V AC power supply (via autotransformer) was 80 Gauss (0.0080 Tesla).

The resultant electromotive force according to equation 1 is:

$$\begin{aligned} F &= qE + ilB \\ &= (1.6 \times 10^{-19}) \left( \frac{45}{0.04} \right) + (0.410)(0.04)(0.008) \\ &= 1.8 \times 10^{-16} + 1.312 \times 10^{-4} \\ &\approx 1.312 \times 10^{-4} \text{ N} \end{aligned}$$

Due to a low magnitude of this force, we have attempted to increase the magnetic field by increasing the coil current. This can be done by three methods,

- 1) Frequency Method: By changing the frequency to approach the natural resonance frequency.
- 2) Resonance Method: Placing additional reactance in the circuit will lower the resonance frequency to 60Hz.
- 3) Voltage Method: By increasing the AC voltage to kV range

Due to unavailability of variable frequency and high voltage drivers, method 2, was chosen.

### 4.3.1 Resonance Method

Placing additional reactance and capacitive reactance in the circuit will neutralize the coil reactance, so that the power will be transmitted as there was no reactance at all. This is

called resonance. When the circuit contains both inductive and capacitive reactance in series with resistance, the impedance can be calculated by first subtracting the capacitive  $X_C$  from the inductive reactance and then combining the resulting reactance  $(X_L - X_C)$  with the resistance [45]. This is shown in Figure 4.10. Equation 4.5 represents the impedance in ohms in term of  $Z$  :

$$Z = \sqrt{R^2 + (X_L - X_C)^2} \quad (4.5)$$

When both of the capacitive and inductive reactance combines in series, the combined effect is the difference between them [46]. This is expressed in the equation

$$\begin{aligned} X &= X_L - X_C && \text{but when} && X_L = X_C \\ 2\pi fL &= \frac{1}{2\pi fC} \\ \therefore f &= \frac{1}{2\pi\sqrt{LC}} \end{aligned} \quad (4.6)$$

The circuit is said to be in resonance, and the current reaches has its maximum value. By comparing the DC and AC system, for DC: 30V supply would have 3A and for AC: system 240V for 0.54A going through the electromagnet. To have a higher magnetic field for the AC case we need to use the above method to increase the current going through the coils.

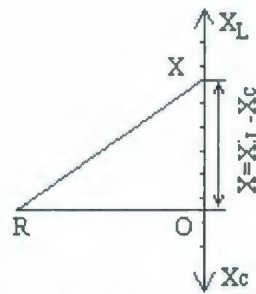


Figure 4.10: Impedance of resistance, inductance, and capacitance in series.

The inductance of the coils is measured with LCR Meters (RLC Meters) to be  $275\text{ mH}$  and the capacitance that should be in series is found to be:

$$C = \frac{1}{\omega^2 L}$$

$$C = \frac{1}{(2\pi f)^2 (275 \times 10^{-3})}$$

$$\therefore C = 0.255 \times 10^{-6} \text{ F}$$

The value of  $25.5\text{ }\mu\text{F}$  is a theoretical value and an experimental verification was conducted. Variable capacitance was placed in series with the inductance as shown in Figure 4.11. Table 4.3 shows the resulting values.

As it can be observed from the experimental part, the value of resonance capacitance is different with the experimental value. Value of  $9.72\text{ }\mu\text{F}$  was selected to obtain the resonance.

The maximum coil current is  $9.51\text{ mA}$  that gave the equivalent magnetic field of  $0.012\text{ T}$ , demonstrating in Figure 4.14. This value is about 17 times less than DC magnetic field.



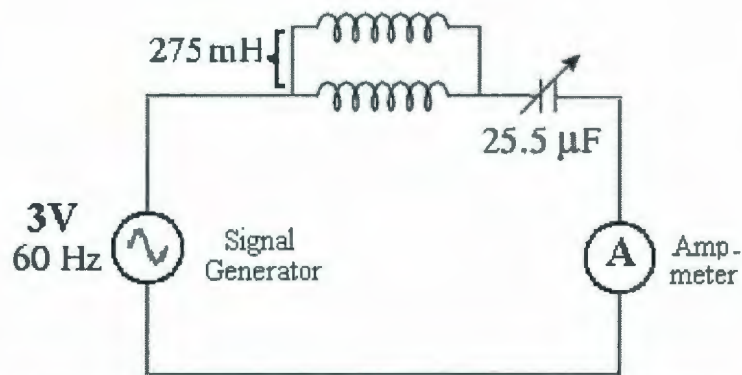


Figure 4.11: Configuration to find resonant of the circuit

The resulting Lorentz force obtained using the AC method was in the order of  $10^{-3}$  compared to the gravitational force. In order to visualize the effect of the Lorentz force, a hundred times  $10^{-2}$  stronger magnetic field is still needed for which the instrumentation was not available.

Capacitance( $\mu F$ )	Current( mA )
2.2	1.87
6.35	7.28
8.66	9.44
<b>9.72</b>	<b>9.51</b>
9.8	9.49
14.6	9.4
21	9.3
22.9	9.13
25.5	8.8
26.6	8.86
30.1	8.8
52.8	7.91
100	7.6
142	7.41
270	7.23

Table 4.3: Experimental values for resonant.

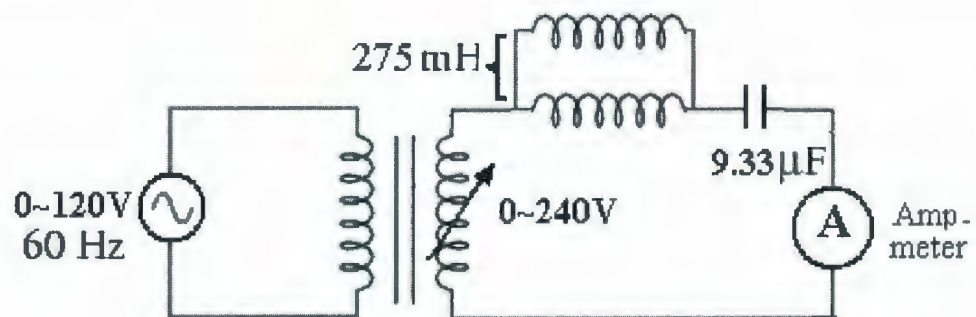


Figure 4.12: Configuration of the resonant circuit.

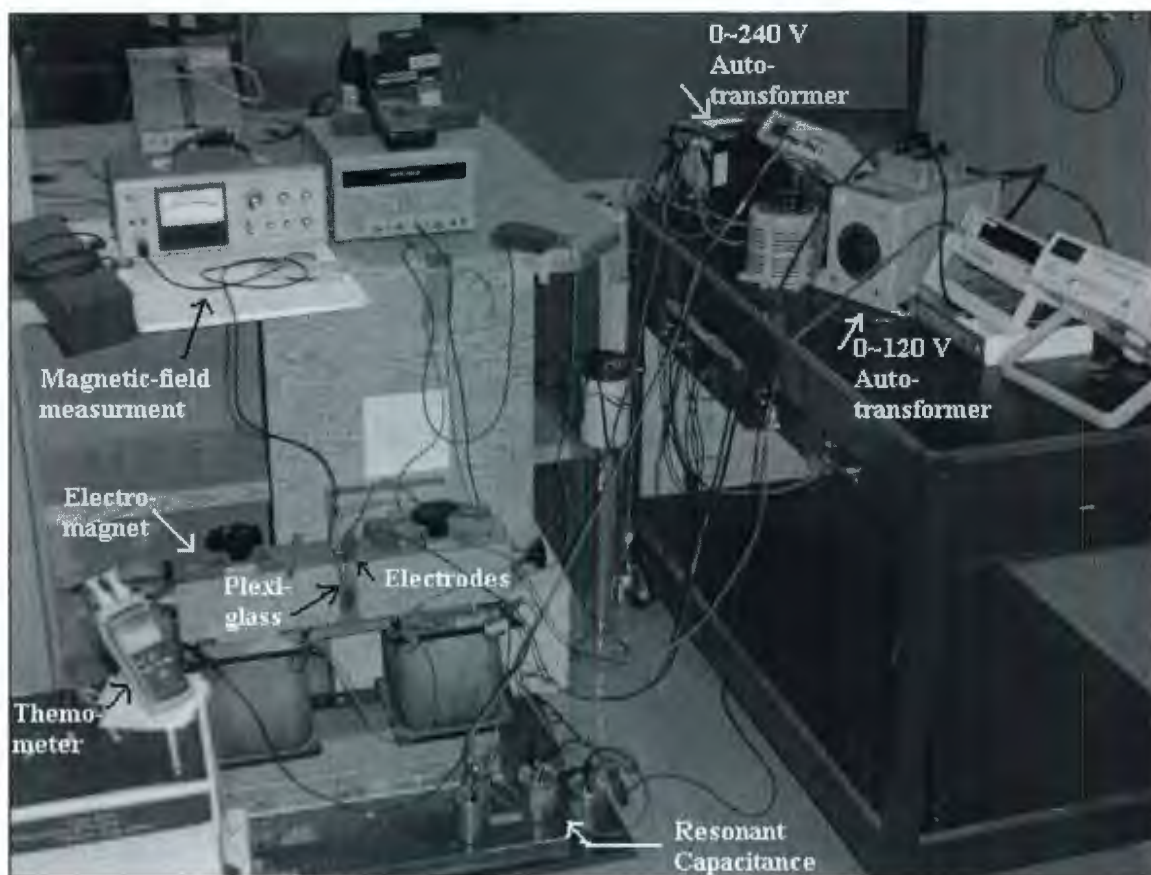


Figure 4.13: The experimental view of the AC mode.

## 4.4 Concluding Remarks

Using the concept of Lorentz force to separate oil from water, the experiment was carried out with the largest electromagnet at Memorial University. The electromagnet was powered with DC and AC power, however the resulting force field was very low. Different methods for increasing the current through the coils were conducted; however, the magnitude was still low and the electromagnetic force was not able to accelerate non-conductive particles (oil) at the desired speeds.

The DC system in addition established an unwanted electrolysis formed near the electrodes. In order to make the system applicable to the industry, we would need either

1. A strong DC magnetic field with large currents and rapid flow to prevent the hydrolysis, or
2. A strong AC magnetic field which would require a very high voltage and possibly a variable frequency AC power supply.

Due to the unavailability of the strong electromagnet, a mechanical separator was designed which is the topic of next chapter.

## Chapter 5

### Stratifying the Multiphase Flow Using a Hydrocyclone

In order the measurement is independent of the flow regime, we propose using a novel cyclone device which spins the multiphase flow and forms a stratified flow due different densities of the oil and water in the crude oil. Consequently a new cavity sensor is designed to measure the capacitances of the flow (Chapter 6).

Common cylindrical hydrocyclones are vertical pipes with a horizontal inlet that helps oil-water separation to occur. The liquid phases enter the vertical separator section through a reducing area nozzle, increasing their velocity. The swirling motion in hydrocyclone produces a centrifugal force, whereby, water (higher density liquid) keeps the outer wall and oil (lower density liquid) near the outer of the hydroclone. Due to the geometry of hydrocyclone, oil stream exits through the top overflow and water stream leaves the system through the bottom underflow.

By using the principle rule of hydrocyclone, the new model is designed to use the concept of centrifugal force to separate oil from water. This separation stratifies the flow into two



layers of water and oil. The flow enters hydrocyclone body, the swirling motion is produced, and centrifugal force makes the higher density material, water, to move to the surface edges while the lower density, oil, to the inner part of the new designed hydrocyclone.

Most hydrocyclones are having the underflow orifice smaller than the overflow diameter; therefore, only a fraction of the feed liquid escapes through the underflow, carrying the denser particles. The remaining flow reverses its vertical direction and goes up and out through the overflow pipe, carrying the lighter density particles Figure 5.1.

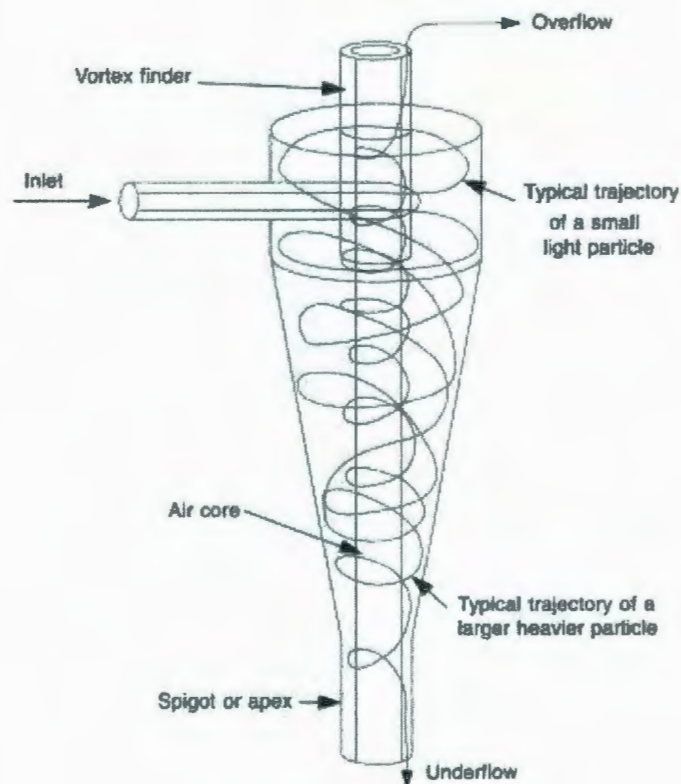


Figure 5.1: Schematic view hydrocyclone [25]

In our design, the hydrocyclone geometry is designed to carry all the flow through underflow diameter. Therefore the stratified output flow from the new designed hydrocyclone can enter the capacitance sensor for measurement purposes. Figure 5.1 shows the passage of the fluid inside the proposed hydrocyclone, the inner helical path carries oil and the outer helical path carries water such that the output flow is stratified. The main difference of this hydrocyclone with the other hydrocyclones is the overflow pipe. Overflow pipe is eliminated and the underflow diameter is designed to carry the entire input flow through it.

Another important parameter in the Hydrocyclone geometry design is the configuration of the inlet. The main goal is to inject the fluid with high tangential velocity. To generate the tangential velocity the inlet is designed to be attached at a small angle to the main body.

## 5.1 System Configuration

Different geometrical configurations have been studied; the most popular ones are Rietema, Bradley and the Dabir's hydrocyclones.

All of them are conceptually similar with differences only in relative dimensions. Our model is based on Dabir's Hydrocyclone as illustrated in Figure 5.2.

The designed model consists of four main parts:

- 1) Inlet Part: Flow enters the body of hydrocyclone with an  $\theta$  angle to create a higher tangential velocity.
- 2) Cylindrical Part: Cyclone operation is initiating

- 3) Conical Part: Centrifuge force separates oil from water, water particles move to wall part and oil to the inner surface of the conical section and the
- 4) Underflow Part: Stratified flow leaves the hydrocyclone and enters the measurement sector.

The hydrocyclone has the inside diameter of the cylindrical section **D** of 85mm as illustrated in Fig.5.3. Like the referenced designs [24, 27, 48] the value of each segments are expressed in term of **D**. The inlet diameter of the system is designed to be  $0.28D$  ( $\approx 22mm$ ) which is the standard pipe size of  $3/4$ " inch. The heights of cylindrical and conical part are  $L_1$  and  $L$  respectively and the inlet is at an angle ( $\theta=5^\circ$ ). The outlet diameter of the system has the same diameter as the inlet.

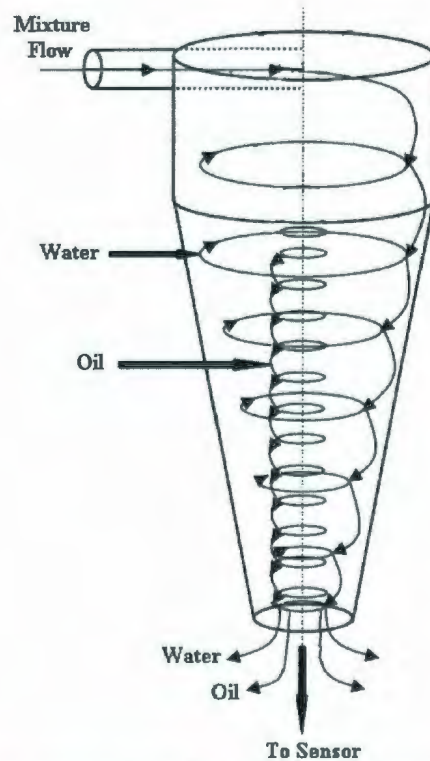
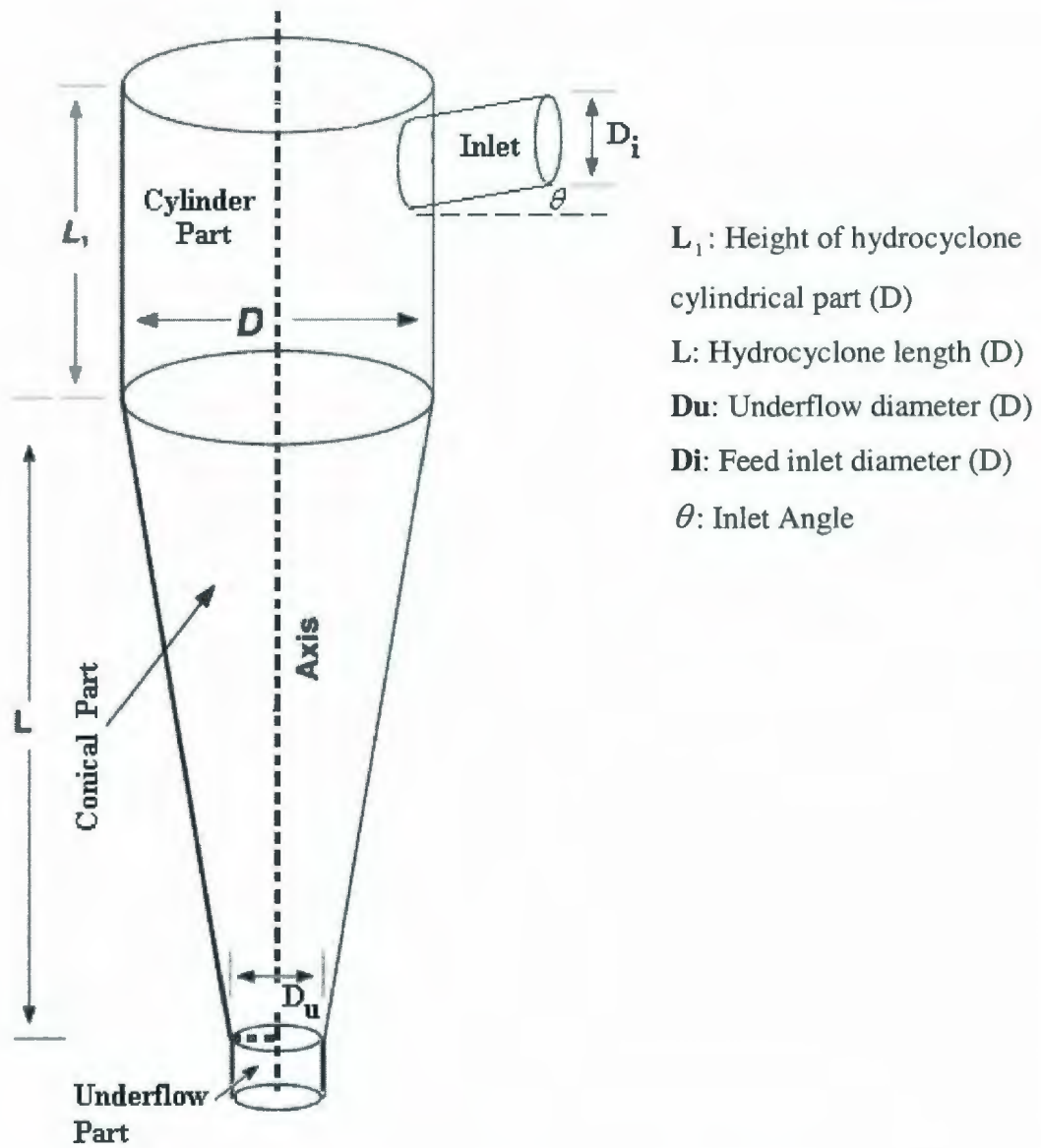


Figure 5.2: Schematic view of the fluid flow inside the new hydrocyclone



L	L1	Di	Du	$\theta$
4.1D	1.44D	0.28D	0.28D	5°

Figure 5.3: Geometrical configuration of the hydrocyclone

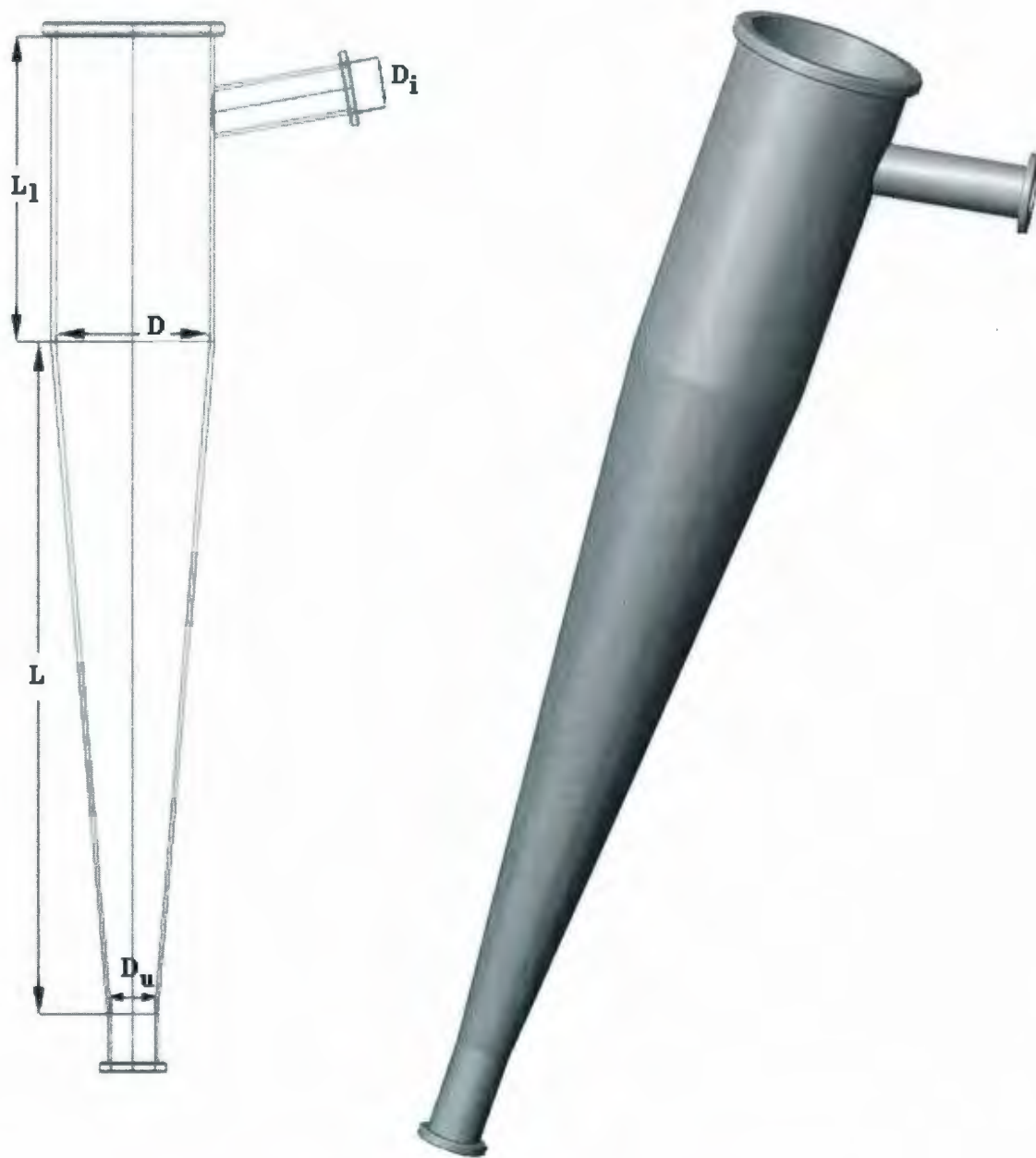


### 5.1.1 System Fabrication

Our hydrocyclone was fabricated in Memorial University's glass-blowing shop. The 22mm Inner diameter (with 26mm Outer diameter) glass pipe was attached at an angle of  $5^{\circ}$  to the cylindrical part of 85mm in diameter. Figure 5.4 shows after dimensions of the hydrocyclone.

Since the output section of the hydrocyclone feeds to designed sensor, the outlet is terminated by a flange, shown in Figure 5.5.

Figure 5.6 shows the complete hydrocyclone with a stand.



L(mm)	L1(mm)	Di(mm)	Du(mm)	$\theta$
349.25	158.75	22	22.5	5°

Figure 5.4: Actual configuration of the designed hydrocyclone after fabrication.

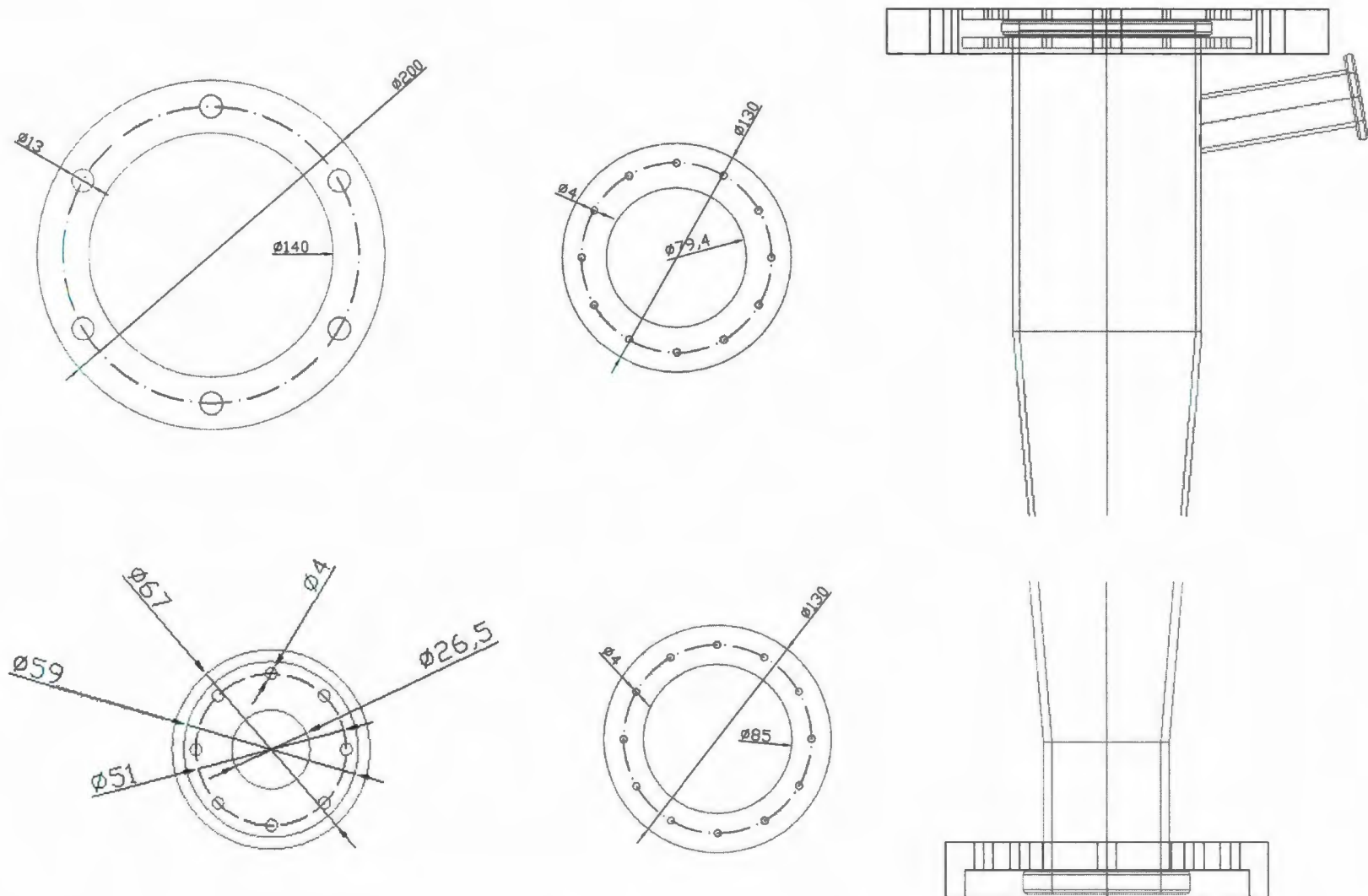


Figure 5.5: Flanges that are attached to the system.



Figure 5.6: Final Schematic of the Hydrocyclone.



## 5.2 The Sensor Design

We designed a cavity sensor to measure the volumetric ratio of two liquid phases by using the capacitance technique. Capacitance sensors are widely used due to their simplicity and low cost [7] in accurate distance measurements [49], or liquid level measurement [50]. Capacitance sensors come in different configurations, such as parallel plates, concave plates, or double helix designs.

The capacitance between two electrodes is generally sensitive to flow regimes due to the non uniformity of the electric field within the measurement area; however with the use of “hydrocyclone” (previous chapter), the flow is stratified<sup>2</sup> before entering the measurement area (sensor).

The capacitance measurement depends not only on the volumetric ratio but also on different water and oil permittivities. In our case we consider a range of water permittivity:  $\epsilon_{water} = 75 - 85$  and for oil permittivity  $\epsilon_{oil} = 2.5 - 3.5$ . To simplify the calculations, three representative permittivities are used:  $\epsilon_{water} = 75, 80, 85$  and  $\epsilon_{oil} = 2.5, 3.0, 3.5$ . The capacitance measurement is thus dependent only, the water permittivity ( $\epsilon_{water}$ ), the oil permittivity ( $\epsilon_{oil}$ ) and the volumetric ratio ( $\alpha$ ).

---

<sup>2</sup> If the multiphase flow is in a form of emulsion, the separation/stratification will not occur. The measurement should recognize this situation.

## 5.2.1 Design Objectives

The main objective of the design is to build a sensor that would be capable of measuring volumetric ratio precisely. The sensor should be non-intrusive in order to avoid any changes to the flow characteristics. It should also be capable of measuring the entire ranges of volumetric ratio, ranging from 0% to 100% of oil in water, each of varying permittivity.

## 5.2.2 Design Consideration

The capacitance sensor measurement is affected by two major factors:

1. The geometry and shape of the electrodes in the sensor
2. The dielectric between the electrodes and stray capacitances

### 5.2.2.1 The geometry and shape of the sensor

The formulation of our sensor is to measure the volumetric ratio independently of water and oil permittivities. The capacitance measurement is generally a function of three unknowns:

$$C = f (\epsilon_{water}, \epsilon_{oil}, \alpha) \quad (5.1)$$

In order to eliminate  $\epsilon_{water}$  and  $\epsilon_{oil}$  from the formula we need to supply two additional measurements:

$$C_1 = f (\epsilon_{water}, \epsilon_{oil}, \alpha)$$

$$C_2 = f(\epsilon_{\text{water}}, \epsilon_{\text{oil}}, \alpha) \quad (5.2)$$

$$C_3 = f(\epsilon_{\text{water}}, \epsilon_{\text{oil}}, \alpha)$$

Also, it is required that  $C_1, C_2, C_3$  are linearly independent. By placing three electrode-pairs in different locations within the sensor, three linearly independent measurements can be achieved. However the electrodes should be located in a close proximity to each other to ensure the same flow conditions are present at each electrode-pair.

First, to maintain the flow velocity at a constant rate the cavity between each electrode pairs must have the same cross-sectional area. The velocity of the flow will thus be approximately equal within the whole measurement volume to keep the flow regime unchanged.

The ideal shape of the measurement volume that seamlessly interfaces with the hydrocyclone operation is found to be a ring cavity within a funnel. Ring electrodes provide a higher sensitivity and stronger signal to concave plate electrodes.

#### 5.2.2.2 Employing the guard electrodes

One of the problems associated with capacitance measurement is fringing [4]. Fringing is when the electric field lines travel outside of the area between the electrodes and the field is not uniformized. The distance between the electrodes will determine how much fringing of the electric field occurs. If the distance between the electrodes is small relative to the area of the electrodes, the fringing is minimal, and therefore this will not affect the capacitance measurement result. However, in our sensor the distance between the electrodes is rather large determined by the sensor's geometry.



As a result, guard electrodes are needed to to reduce fringing. The purpose of the guard electrodes is to “drain off” the fringing electric field lines so that they do not affect the capacitance measurement [13].

Elkow and Rezkallah [51] determined several experiments for different capacitance sensors. Based on their results, they found that guard electrodes should be of equal length with the measuring electrodes.

Both the guard electrodes and measuring electrodes should be insulated with distance between them larger than the separation of the measuring electrodes.

### 5.2.3 Mechanical Dimensions

The new cavity sensor of hydrocyclone shape is designed to have constant cross section area within entire cavity. A schematic of the new sensor that meets the above criteria is shown in Figures 5.6 and 5.7. The sensor consists of an inner cone and outer funnel providing the required cavity shape.

The inner part of the sensor has a conical shape and consists of PVC (polyvinyl chloride or vinyl) with inlet radius of 0mm (sharp point), outlet radius of 19.5mm and height of 140mm. The outer part of the sensor is made from aluminum with inlet radius of 11.25mm, outlet radius of 22.5mm and height of 140mm. These dimensions are illustrated in Figure 5.7. The inner part of the sensor is conical shape with angle of  $7.9^\circ$ , however to have the equal cross section area the outer part of sensor has a hyperbolic geometry that is plotted in Figure 5.9.



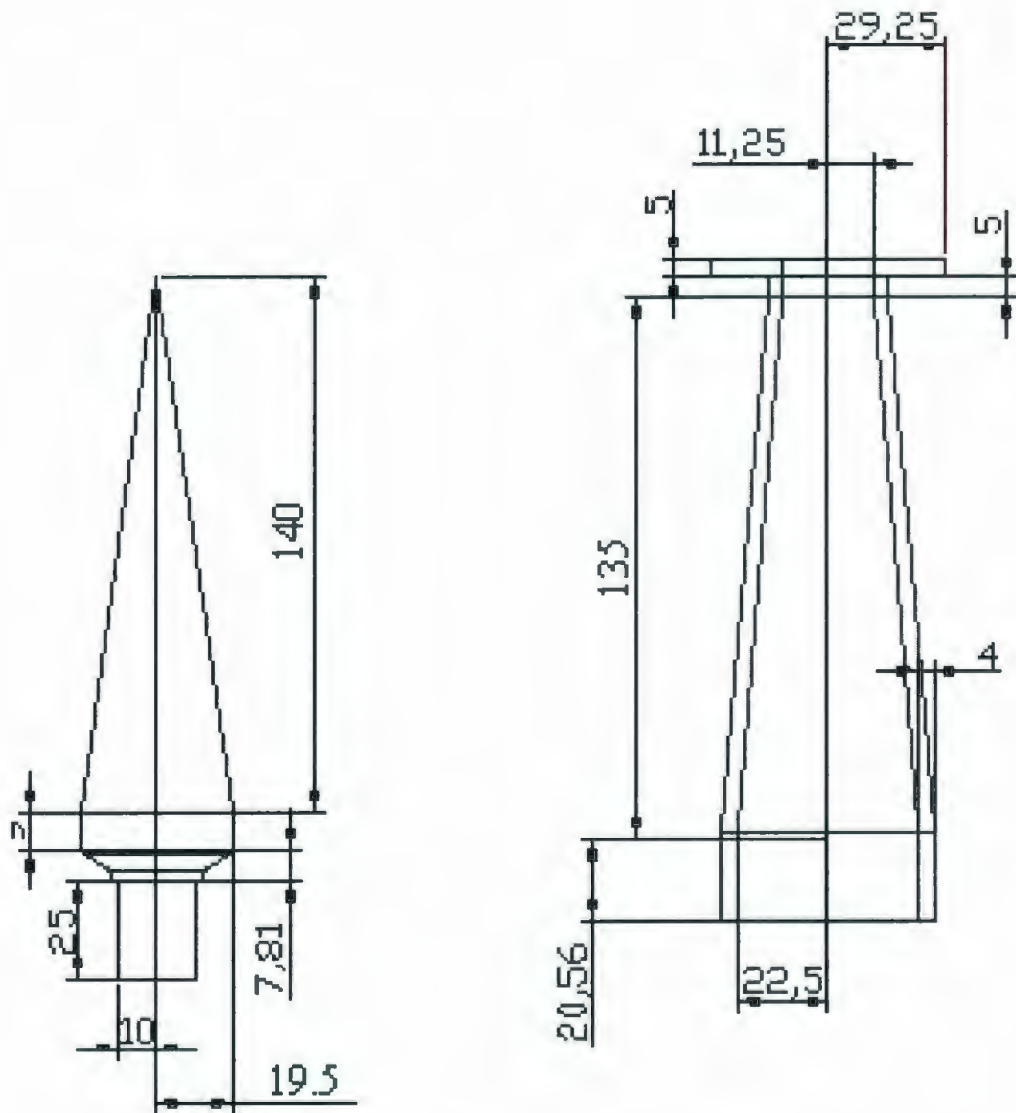


Figure 5.7: Cross section of the inner and outer part of the new designed sensor.

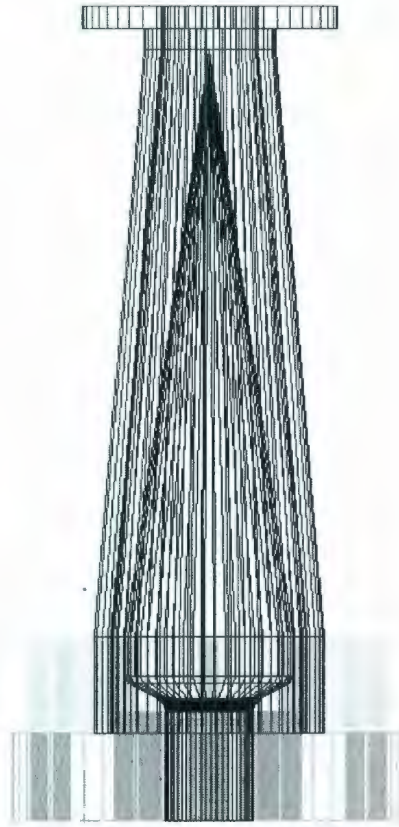


Figure 5.8: Schematic of the new designed capacitance sensor

The 2D profile of the inner cone is (shown in red Figure 5.9)

$$x = -\frac{19.5}{140}y + 19.5 \quad (5.3)$$

and the outer layer's hyperbolic equation is (shown in Figure 5.8, blue color)

$$x = \sqrt{(11.25)^2 + \left(\frac{19.5}{140}y + 19.5\right)^2} \quad (5.4)$$

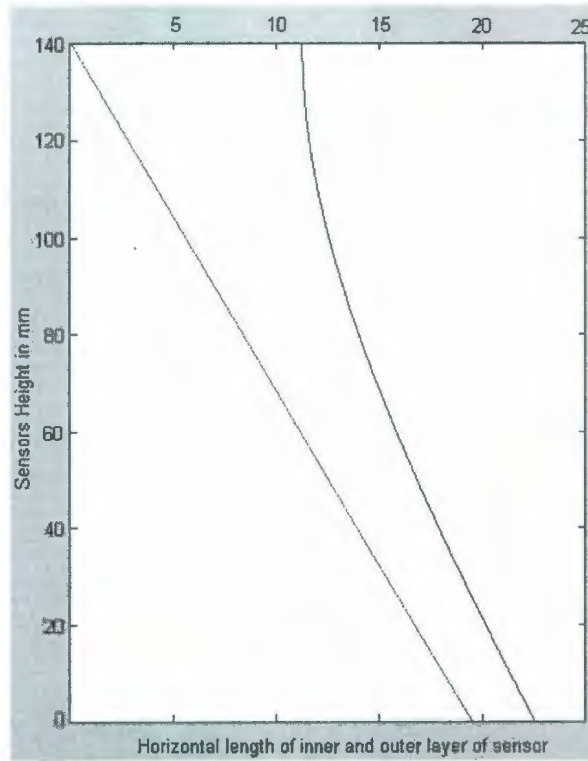


Figure 5.9: 2D Plot of Inner and outer layer of the designed sensor

The 3-Dimension schematic of the sensor is sketched using AUTOCAD software. The sensor is constructed and machined in Technical Service of Memorial University. The inner part is made from PVC and the outer part is from brass material. The reason of choosing brass material for outer surface of sensor is for simplicity of constructing and measuring the capacitances. The three ring-shape electrodes, made of brass sheets, are mounted to the inner surface of the sensor. The three electrodes are 15mm long and 20mm equally spaced from each one on the circumference of the sensor. Since the angle between the inner part of sensor (approximately  $7.9^\circ$ ) and the outer part is very small the capacitance measuring electrodes are approximating as ring electrodes in some of the further result simulations, this is very observable in the outlet regions. Each of the three

measuring electrodes that are mounted to the inner part, are connected to the measuring electrodes “+V” voltage. Conversely the outer surface is connected to “0” voltage (grounded), since the outer surface material is from brass the distribution of 0V will be uniformly constant.

Consequently the three measuring electrodes are surrounded with four ring guard electrodes that are grounded. The guard electrodes with 10 mm length are placed (attached to the surface) 5mm apart from top and bottom of each measuring electrodes in the inner part of conical sensor. They form the ring guard electrode with the outer surface of the sensor. However since the outer part of sensor is entirely connected to ground, 0 voltage, therefore the outer guard electrodes are not attached to the sensor. The four ring guard electrodes ensure that the electric field lines run directly across the sensor and do not experience fringing.

New designed capacitance sensor is drawn with its complete stands in AUTOCAD software. To hold the sensor together and also to attach it to the final system with the designed hydrocyclone the stands with different dimensions and shapes are designed. The stands with the dimensions in mm are shown in Figure 5.10 and Figure 5.11 illustrated the 3-Dimensional image of the designed sensor. Also, the image of the new designed sensor and hydrocyclone with the stands are shown in Figure 5.12.

The complete system containing the new hydrocyclone and the capacitance sensor are put together using the stands. Therefore the designed hydrocyclone stratifies the flow and the capacitance sensor measures the volumetric ratio of oil in water. Now the model is ready for the simulations that are discussed in the following chapter.



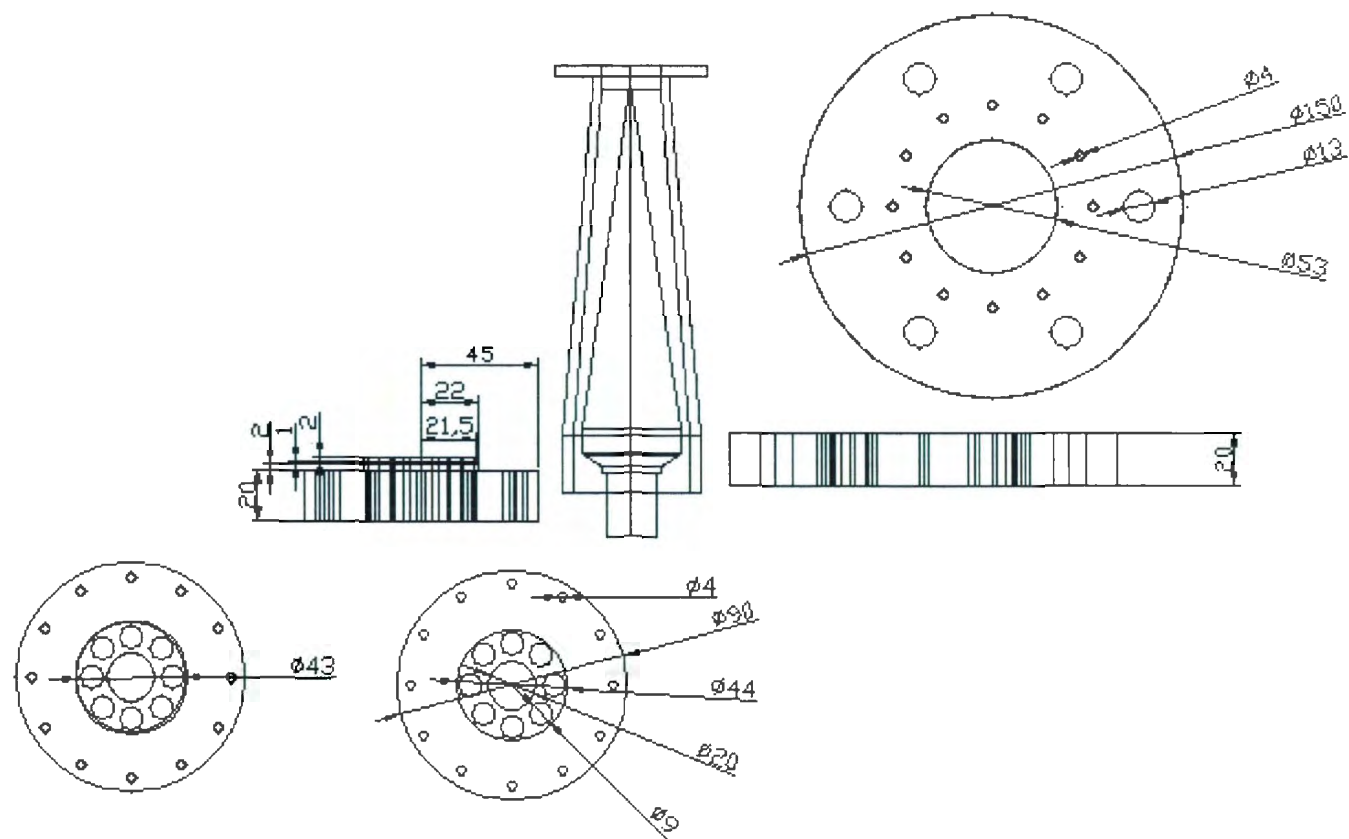


Figure 5.10: New designed sensor with the stands dimensions



Figure 5.11: Designed capacitance sensor.



Figure 5.12: Designed capacitance sensor and the hydrocyclone.

## Chapter 6

### Numerical Modeling

Finite Element Method (FEM) is a numerical procedure that can be used to obtain solutions to a large class of engineering problem involving, heat transfer, electromagnetism, and fluid flow. With the specific geometry, material properties, and boundary conditions, FEM was used to calculate the electric field intensity distribution and the resulting capacitance of the sensor at the diverse conditions.

The differential equation that governs the relationship between electrical charge and voltage is the Poisson's equation listed below:

$$\epsilon_x \frac{\partial^2 V}{\partial x^2} + \epsilon_y \frac{\partial^2 V}{\partial y^2} + \epsilon_z \frac{\partial^2 V}{\partial z^2} = -\rho \quad (6.1)$$

where  $V$  is the electrical potential,  $\rho$  is the volume charge density within the dielectric material,  $\epsilon_x, \epsilon_y$  and  $\epsilon_z$  are the relative permittivities of the dielectric material in the x, y, and z directions, respectively [53]. Because of the low ionic contaminant in the dielectric



material, the free charge and the polarization charge are assumed to be zero. With this assumption ( $\rho = 0$ ) the electric field  $E$  can be related to the potential gradient as:

$$E = -\nabla V \quad (6.2)$$

The magnitude of the electrical potential energy  $U$  (electrostatic energy) is obtained by integration of the dot product of the electric field ( $E$ ) and electric displacement ( $D$ ) over the volume of the system as shown below:

$$U = \frac{1}{2} \int_v E \cdot D \, dv \quad (6.3)$$

, where

$$D = \epsilon E \quad (6.4)$$

The capacitance of the concentric electrode pair can then be calculated using equation (6.5) where  $(V_1 - V_2)$  is the voltage differential the electrodes, and  $U$  is the electrostatic energy to sum the energies for the element in order to obtain the electrostatic energy, and the capacitance.

$$C = \frac{2U}{(V_1 - V_2)^2} \quad (6.5)$$

## 6.1 Software Implementation

FEM software includes three main parts: pre-processing, solution and post-processing.

Pre-processing consists of the following

Steps:

1. Subdividing the problem into nodes and elements.
2. Defining the element type.
3. Defining material properties.
4. Developing equations for an element.
5. Defining analytical geometry model.
6. Applying boundary conditions, initial conditions, and loading conditions.

In the Solution phase,

A set of linear or nonlinear algebraic equations are solved simultaneously to obtain nodal results.

In the Post-processing, the results are converted into a desired form and displayed/plotted graphically.

Since our model is 3-D, the 10-node tetrahedral elements were selected for meshing operation (Figure 6.1).




PLANE121		Dimensions: 2-D <i>Shape or characteristic:</i> Quadrilateral, 8 nodes <i>Degrees of freedom:</i> Voltage at each node
SOLID 122		Dimensions: 3-D <i>Shape or characteristic:</i> Brick, 20 nodes <i>Degrees of freedom:</i> Voltage at each node
SOLID 123		Dimensions: 3-D <i>Shape or characteristic:</i> Tetrahedral, 10 nodes <i>Degrees of freedom:</i> Voltage at each node

Figure 6.1: Finite element for an electrostatic analysis

The ANSYS program can automatically generate the nodes and elements, once the element attributes are selected and the element size is defined.

Element attributes include element type(s), and material properties, while the element size controls the fineness of the mesh. The smaller the element size, the finer the mesh. In our models we used the meshing size of 3.

Subsequently the FEM analysis involves applying appropriate boundary and loading conditions. The loads and boundary conditions can be applied in 3-D electrostatic analysis either as key points, lines, and/or areas, or the conditions can be directly imposed on the nodes and elements. In our case, the first approach is chosen because should we decide to change the meshing, we will not need to update boundary conditions and the loads. Also, our load and boundary conditions are voltages that are applied to surfaces.

Once we have created the model and have applied the boundary conditions loads, then ANSYS solves a set of equations generated by the model, and displays the voltage distribution. Finally, each capacitance is then evaluated.

## 6.2 Simulation

### 6.2.1 Cylinder model

In order to verify the accuracy of our FEM simulation, initially, we simulated a ring electrode system, which we compared to the calculated values from analytically obtained formula.

We modeled a 3D FEM cylinder model depicted by Figure 6.2. The outer ring electrode is grounded while inner electrode is at potential 10V, and the dielectric between is air of

relative permittivity of  $\epsilon_{air} = 1$ . The model is assumed ideal so the fringing is neglected. Therefore, the software repeatedly calculates the electric potentials of all nodes until it satisfies the required degree of accuracy. The electric field and electric flux density are therefore calculated from the electric potentials.

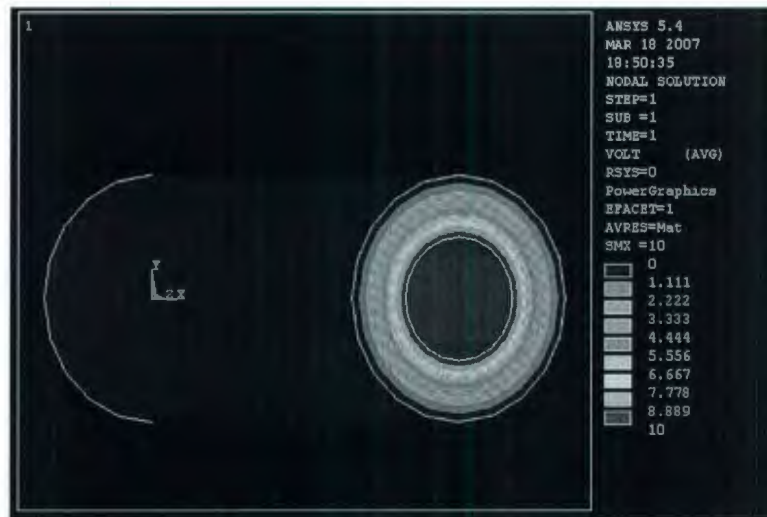


Figure 6.2: Schematic of the cylinder model in ANSYS.

After comparing these results to the capacitance of conductive cylinders, the modeling error is found to be 0.03%.

## 6.2.2 Sensor modeling

The sensor's geometry is divided into small elements that are connected to form the final 3D model. The stray/guard capacitances are placed between the pick up electrodes and their effect is discussed below.

The sensor cavity is designed to guide the high density liquid (water) near outer electrode and the lower density liquid, oil, near the inner electrode. Figure 6.3 shows the case of



50% oil and 50% water. Depending on value of  $\alpha$  (percentage of oil content), the dielectric is divided into two sections, with the interface radius of  $R_o$ .

$$A_{Total} = (R_2^2 - R_1^2)\pi \quad (6.2)$$

$$A_{oil} = (R_o^2 - R_1^2)\pi \quad (6.3)$$

$$A_{water} = (R_2^2 - R_o^2)\pi \quad (6.4)$$

$$\alpha \% = \frac{A_{oil}}{A_{Total}} \times 100\% \quad (6.5)$$

1. Flow regime of the two-phase flow does not change along the sensor's axis.
2. Permittivities of individual phases remain constant.

Here, we assume the oil content  $\alpha$ , the flow regime, and the dielectric permittivities  $\epsilon_o, \epsilon_w$  to be constant across the sensor's length at each sampling interval.

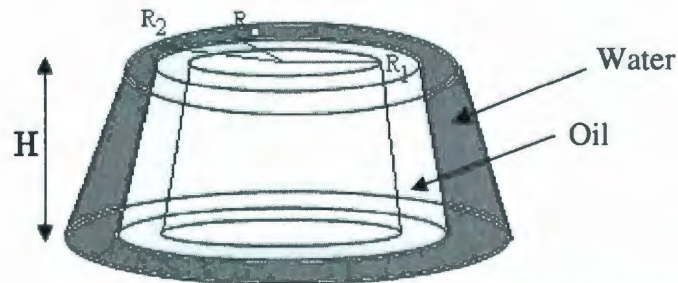


Figure 6.3: Cross section of one of the capacitances without guard electrodes

## 6.3 Evaluation for need of FEM

An analysis has been conducted to assess the need of using FEM. We compared conductive cylinder model to FEM model of curved electrodes for the dielectric being air, and no guard electrodes.

The three cylindrical segments have the closest dimensions to the real curved segments. The inner and outer radius of each cylinder is calculated to be the average radius of the top and the bottom radii electrode.

Table 6.1 shows the comparison which reveals that  $C_2$ , and  $C_3$  FEM model is very close to the analytical capacitance. However  $C_1$ , has large discrepancy since the dimensional shape is quite different to the cylinder shape. For this reason, the use of FEM is justified.

	<b>Analytical Capacitance</b>	<b>FEM Capacitance</b>
<b>C1</b>	0.432	0.6857
<b>C2</b>	1.376	1.393376
<b>C3</b>	2.509	2.517

Table 6.1: Comparison table of cylinder equation and our sensor for each capacitances.

Fig 6.4: FEM C1

Height of 15mm  
 Inner electrode=10V  
 Outer electrode=0V  
 No guard electrode  
 Relative permittivity,  $\epsilon_{air} = 1$   
 $R_1 = 2.8mm$  ,  $R_2 = 12.8mm$   
 $R'_1 = 5mm$  ,  $R'_2 = 14.1mm$



Fig 6.5: FEM C2

Height of 15mm  
 Inner electrode=10V  
 Outer electrode=0V  
 No guard electrode  
 Relative permittivity,  $\epsilon_{air} = 1$   
 $R_1 = 8mm$  ,  $R_2 = 16mm$   
 $R'_1 = 10mm$  ,  $R'_2 = 17mm$

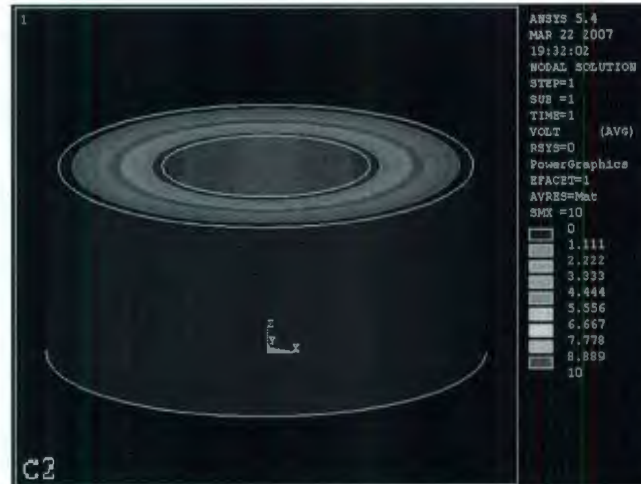
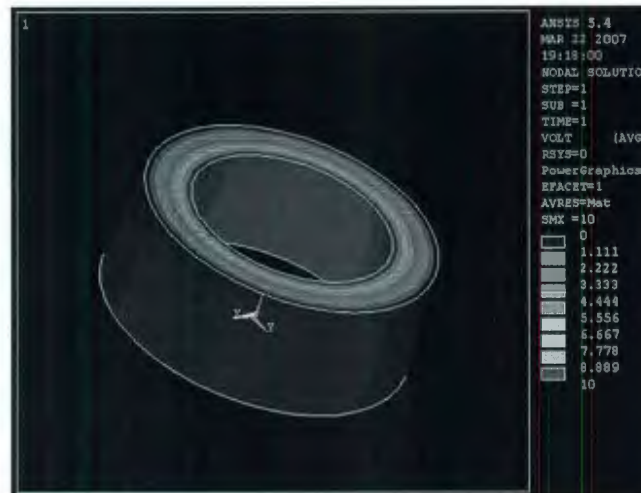


Fig 6.6: FEM C3

Height of 15mm  
 Inner electrode=10V  
 Outer electrode=0V  
 No guard electrode  
 Relative permittivity,  $\epsilon_{air} = 1$   
 $R_1 = 12.6mm$  ,  $R_2 = 18.5mm$   
 $R'_1 = 14.8mm$  ,  $R'_2 = 19.8mm$



### 6.3.1 Model with Guard Electrodes

Each measuring electrode requires a pair of guard electrodes on each side to reduce fringing. Guard electrodes “drain” the fringing electric field lines so they do not affect the capacitance measurements. Comparison of the model with and without guard electrodes was evaluated and the result is shown in Table 6.2/Fig 6.7. For the dielectric we considered air. The capacitances with guard electrodes are higher as a result.

	With Guard(pF)	Without Guard (pF)
C1	0.9846	0.6857
C2	1.9928	1.393376
C3	3.315	2.517

Table 6.2: Comparison value of capacitances with and without guard electrode

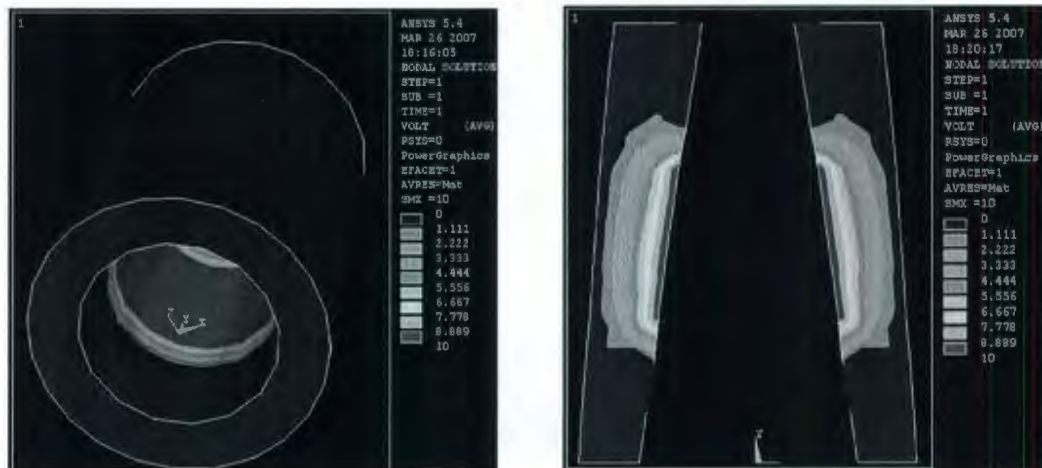


Figure 6.7: Schematic and cross section model of  $C_2$  with guard electrodes.



We also compared the analytical model of the cylindrical electrodes derived by FEM while considering a variable volumetric fraction of oil/oil in water, ranging from 0% to 100% ( $\epsilon_{water} = 80$  and of  $\epsilon_{oil} = 3.0$ ).

The FEM derived values are compared to the concentric cylinders model that meets the following concept:

Calculation of the capacitances is done by using the average radius of each cross section (Eq. 6.5 and Eq. 6.6).

$$C1 = \frac{1}{\frac{1}{C1x} + \frac{1}{C2x}} = 6.36 pF \quad (6.6)$$

$$C1x = \frac{2\pi\epsilon_0\epsilon_o L}{\ln(b/a)} = \frac{2\pi\epsilon_0 3 \times 0.015}{\ln(5.74/4)} = 6.92 pF$$

$$C2x = \frac{2\pi\epsilon_0\epsilon_w L}{\ln(b/a)} = \frac{2\pi\epsilon_0 80 \times 0.015}{\ln(13.5/5.74)} = 78 pF$$

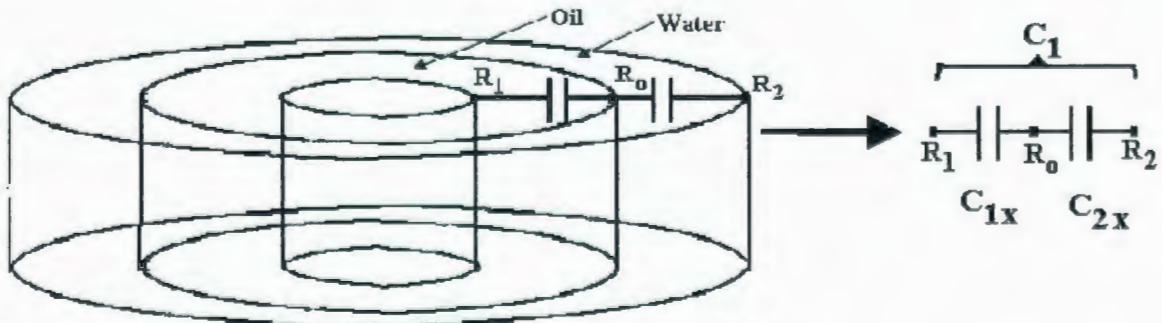
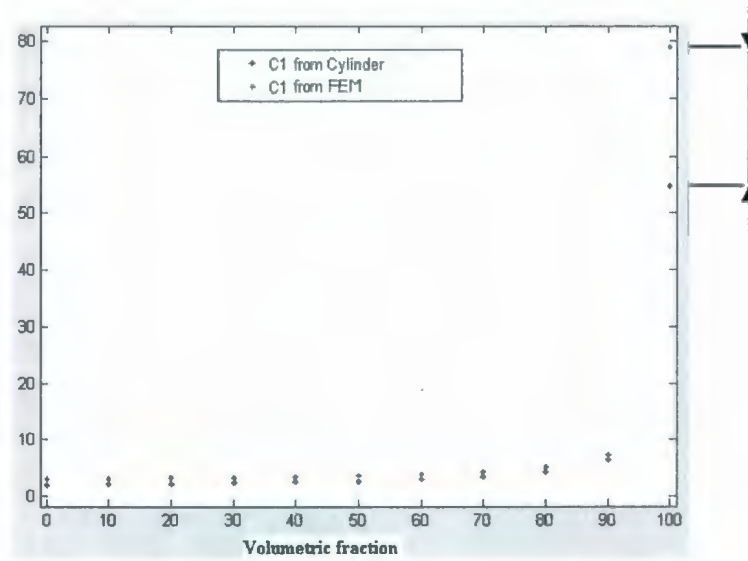


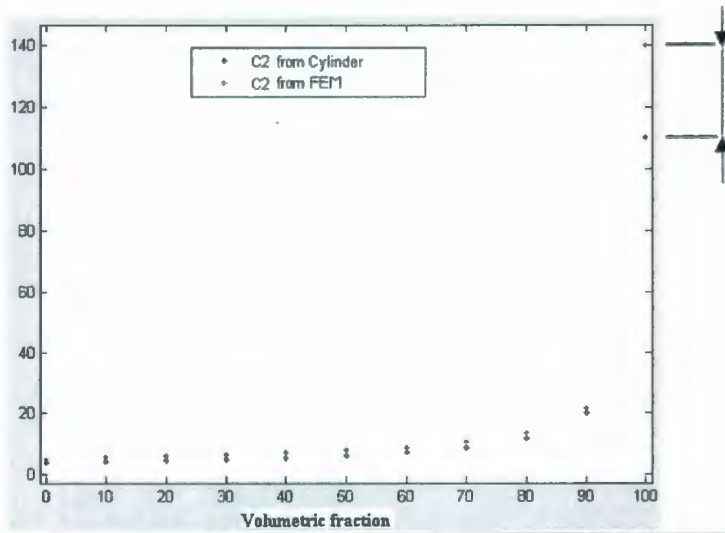
Figure 6.8: Approximation using Concentric Cylinders Model

FEM model capacitances and the approximated capacitances from the Equations 6.6 for each electrode pair are shown in Tables 6.3, 6.4 and 6.5.



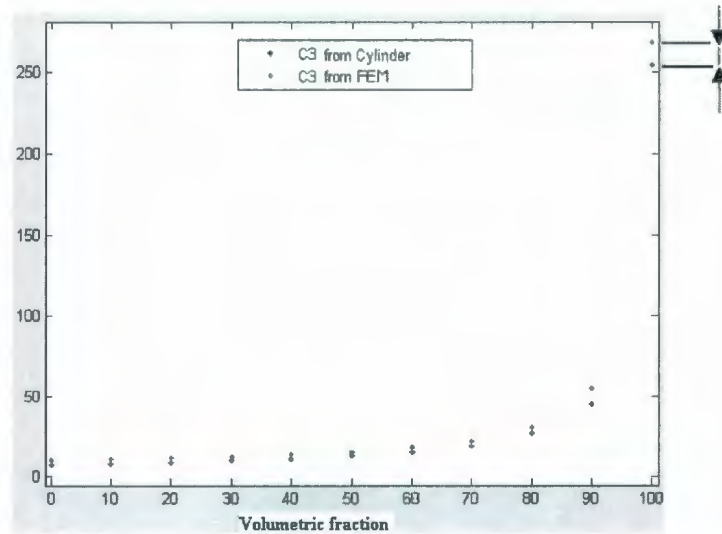
C1	0%	10%	20%	30%	40%	50%	60%	70%	80%	90%	100%
Ansys	2.957	3.0515	3.1738	3.238	3.361	3.571	3.8325	4.287	5.086	7.336	78.86
Cylinder Equation	2.05	2.13	2.23	2.35	2.5	2.69	2.99	3.42	4.23	6.36	54.85

Table 6.3:  $C1 = C_1(\alpha_w)$ ,  $\epsilon_{water} = 80$ ,  $\epsilon_{oil} = 3.0$



C2	0%	10%	20%	30%	40%	50%	60%	70%	80%	90%	100%
Ansys	5.238	5.9761	6.3079	6.7379	7.275	7.954	9.0128	10.583	13.743	21.880	139.690
Cylinder Equation	4.12	4.38	4.69	5.07	5.58	6.31	7.3	8.91	11.98	20.156	110

Table 6.4:  $C2 = C2(\alpha_w)$ ,  $\epsilon_{water} = 80$ ,  $\epsilon_{oil} = 3.0$



C3	0%	10%	20%	30%	40%	50%	60%	70%	80%	90%	100%
Ansyes	10.041	10.906	11.617	12.569	13.707	15.427	18.056	22.108	30.375	55.477	267.78
Cylinder Equation	7.63	8.21	8.98	9.89	11.16	12.87	15.26	19.15	27.03	45.8	254.5

Table 6.5:  $C3 = C3(\alpha_w)$ ,  $\epsilon_{water} = 80$ ,  $\epsilon_{oil} = 3.0$

Analyzing the two approaches, the FEM capacitances are relatively close to the approximated capacitances within the water fraction (water cut) ranging between 0% to 90%. This is attributed to the additional capacitance due to guard electrodes that is part of the FEM model. The region of significant discrepancies is confined into 90% to 100% of water in the volume. However, smaller the ratio of radii ( $\frac{R_2}{R_1} \approx 1$ ) is the case of C3. This is because the ring electrodes become closer to each other thus approaching closer the analytical model.

### 6.3.2 Analysis using variable permittivities

The cross section schematic of the sensor is shown in Fig. 6.9. The sensor has three measuring regions separated by guard electrodes 5mm apart.

Each capacitance was recalculated using three permittivities ( $\epsilon_{\text{water}} = 75, 80 \text{ and } 85$ ;  $\epsilon_{\text{oil}} = 2.5, 3.0 \text{ and } 3.5$ ) in 0-100% of water in the volume for water as well as oil. Tables 6.6, 6.7 and 6.8 list the results that were plotted in Figures 6.10, 6.11 and 6.12

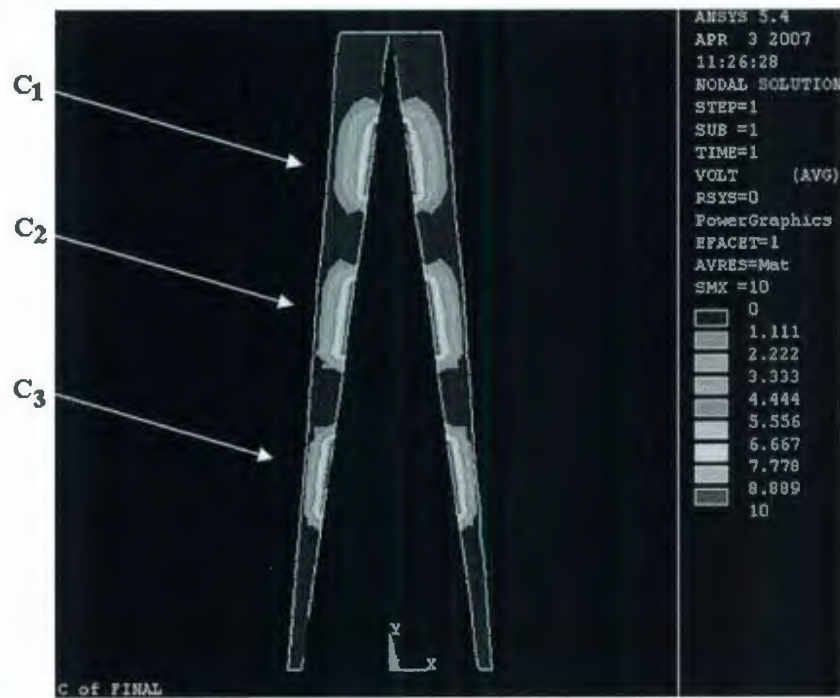


Figure 6.9: Final Schematic



<b>C1</b>	<b>0%</b>	<b>10%</b>	<b>20%</b>	<b>30%</b>	<b>40%</b>	<b>50%</b>	<b>60%</b>	<b>70%</b>	<b>80%</b>	<b>90%</b>	<b>100%</b>
<b>C1 of oil 2.5, water of 75</b>	2.46	2.543	2.6456	2.7000	2.803	2.976	3.198	3.581	4.254	6.158	73.931
<b>C1 of oil 3, water of 75</b>	2.957	3.0513	3.1734	3.237	3.360	3.569	3.828	4.281	5.075	7.304	73.931
<b>C1 of oil 3.5, water of 75</b>	3.45	3.5592	3.700	3.7748	3.915	4.157	4.456	4.977	5.887	8.424	73.931
<b>C1 of oil 2.5, water of 80</b>	2.46	2.5431	2.6459	2.7005	2.8035	2.966	3.2	3.585	4.261	6.181	78.86
<b>C1 of oil 3, water of 80</b>	2.957	3.0515	3.1738	3.238	3.361	3.571	3.8325	4.287	5.086	7.336	78.86
<b>C1 of oil 3.5, water of 80</b>	3.45	3.5594	3.7014	3.776	3.917	4.16	4.461	4.985	5.902	8.466	78.86
<b>C1 of oil 2.5, water of 85</b>	2.46	2.5435	2.6462	2.7010	2.804	2.968	3.202	3.588	4.268	6.201	83.789
<b>C1 of oil 3, water of 85</b>	2.957	3.0517	3.1743	3.239	3.3625	3.573	3.835	4.292	5.096	7.364	83.789
<b>C1 of oil 3.5, water of 85</b>	3.45	3.5598	3.702	3.777	3.919	4.1627	4.465	4.992	5.915	8.504	83.789

Table 6.6: Final simulated values for Capacitance 1.

<b>C2</b>	<b>0%</b>	<b>10%</b>	<b>20%</b>	<b>30%</b>	<b>40%</b>	<b>50%</b>	<b>60%</b>	<b>70%</b>	<b>80%</b>	<b>90%</b>	<b>100%</b>
<b>C2 of oil 2.5, water of 75</b>	4.365	4.995	5.27	5.629	6.08	6.65	7.543	8.87	11.553	18.098	130.96
<b>C2 of oil 3, water of 75</b>	5.238	5.965	6.298	6.727	7.262	7.938	8.989	10.547	13.672	21.643	130.96
<b>C2 of oil 3.5, water of 75</b>	6.111	6.9285	7.318	7.816	8.45	9.212	10.417	12.194	15.733	25.000	130.96
<b>C2 of oil 2.5, water of 80</b>	4.365	5.003	5.278	5.637	6.089	6.662	7.559	8.8966	11.604	18.324	139.69
<b>C2 of oil 3, water of 80</b>	5.238	5.9761	6.3079	6.7379	7.275	7.954	9.0128	10.583	13.743	21.880	139.690
<b>C2 of oil 3.5, water of 80</b>	6.111	6.941	7.330	7.830	8.451	9.233	10.447	12.242	15.827	25.018	139.690
<b>C2 of oil 2.5, water of 85</b>	4.365	5.003	5.284	5.644	6.096	6.672	7.574	8.919	11.65	18.697	148.421
<b>C2 of oil 3, water of 85</b>	5.238	5.986	6.316	6.747	7.286	7.968	9.0334	10.615	13.807	21.998	148.421
<b>C2 of oil 3.5, water of 85</b>	6.111	6.953	7.342	7.842	8.466	9.252	10.475	12.285	15.911	25.265	148.421

Table 6.7: Final simulated values for Capacitance 2.

<b>C3</b>	0%	10%	20%	30%	40%	50%	60%	70%	80%	90%	100%
C3 of oil 2.5, water of 75	8.368	9.092	9.687	10.486	11.442	12.888	15.104	18.522	25.229	47.209	251.044
C3 of oil 3, water of 75	10.041	10.904	11.612	12.560	13.693	15.403	18.015	22.023	30.2	54.75	251.044
C3 of oil 3.5, water of 75	11.715	12.715	13.533	14.627	15.933	17.898	20.891	25.462	34.702	61.806	251.044
C3 of oil 2.5, water of 80	8.368	9.0935	9.69	10.492	11.452	12.905	15.132	18.576	25.684	47.728	267.78
C3 of oil 3, water of 80	10.041	10.906	11.617	12.569	13.707	15.427	18.056	22.108	30.375	55.477	267.78
C3 of oil 3.5, water of 80	11.715	12.718	13.54	14.639	15.951	17.938	20.946	25.563	34.932	62.694	267.78
C3 of oil 2.5, water of 85	8.368	9.094	9.693	10.497	11.461	12.919	15.158	18.623	25.796	48.195	284.516
C3 of oil 3, water of 85	10.041	10.908	11.621	12.576	13.72	15.448	18.092	22.1669	30.531	56.078	284.516
C3 of oil 3.5, water of 85	11.715	12.720	13.545	14.649	15.968	17.958	20.995	25.653	35.139	63.5	284.516

Table 6.8: Final simulated values for Capacitance 3.



Figure 6.10:

$$C = C(\alpha_w, \alpha_{oil}, \alpha_w = 75)$$

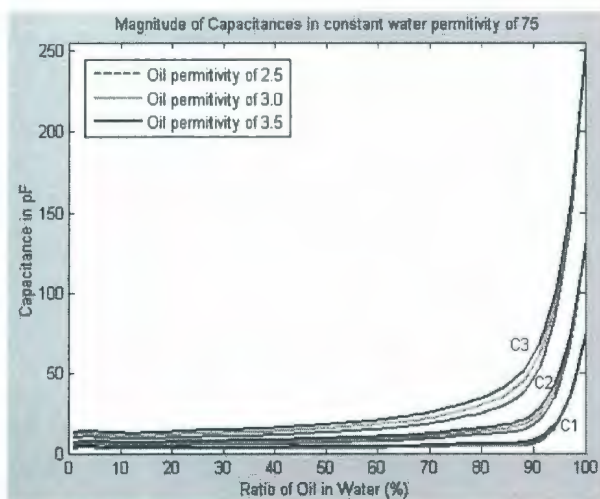


Figure 6.11:

$$C = C(\alpha_w, \alpha_{oil}, \alpha_w = 80)$$

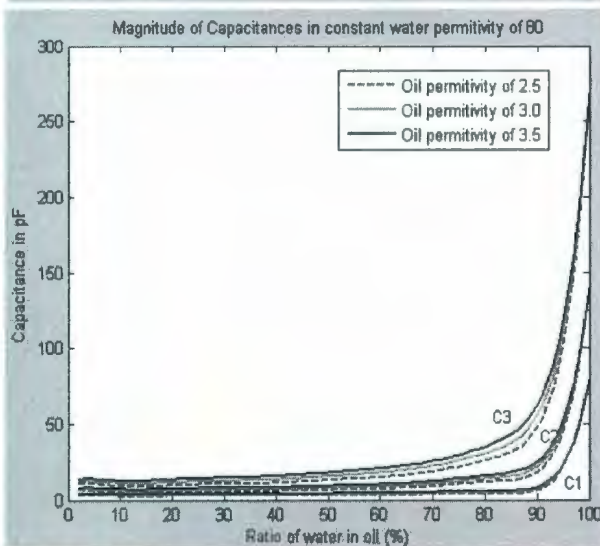
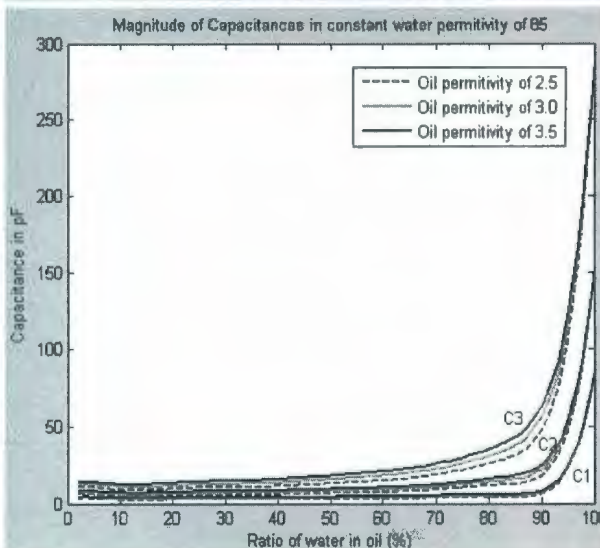


Figure 6.12:

$$C = C(\alpha_w, \alpha_{oil}, \alpha_w = 85)$$





### 6.3.3 Analysis of the 90% to 100% regimes

Capacitances in 0%-90%  $\alpha_w$  region present a close to linear characteristic, which is not

the case for 90%-100% region of  $\alpha_w$  ( $\alpha_w = \frac{V_{water}}{V_{water} + V_{oil}}$ ). To zoom into this region, we

change the independent variable from  $\alpha_w$  to  $\alpha_{oil}$  ( $\alpha_{oil} = \frac{V_{oil}}{V_{water} + V_{oil}}$ ) and use a

logarithmic scale. The plots are re-plotted in Figures 6.13, 6.14 and 6.15.

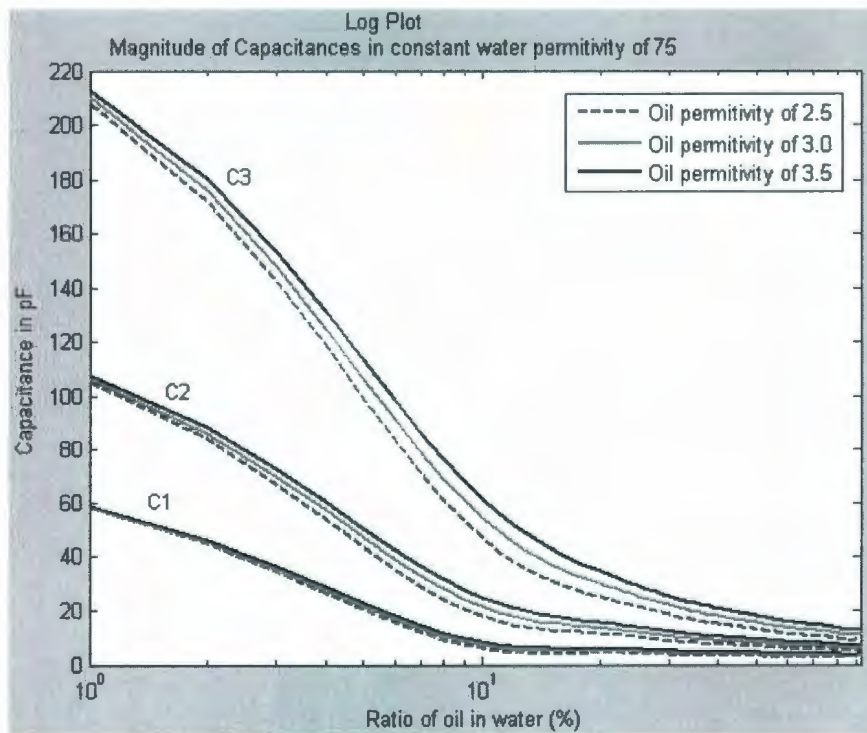


Figure 6.13: Inverse semi-log for  $C = C(\alpha_w, \alpha_{oil}, \alpha_w = 75)$

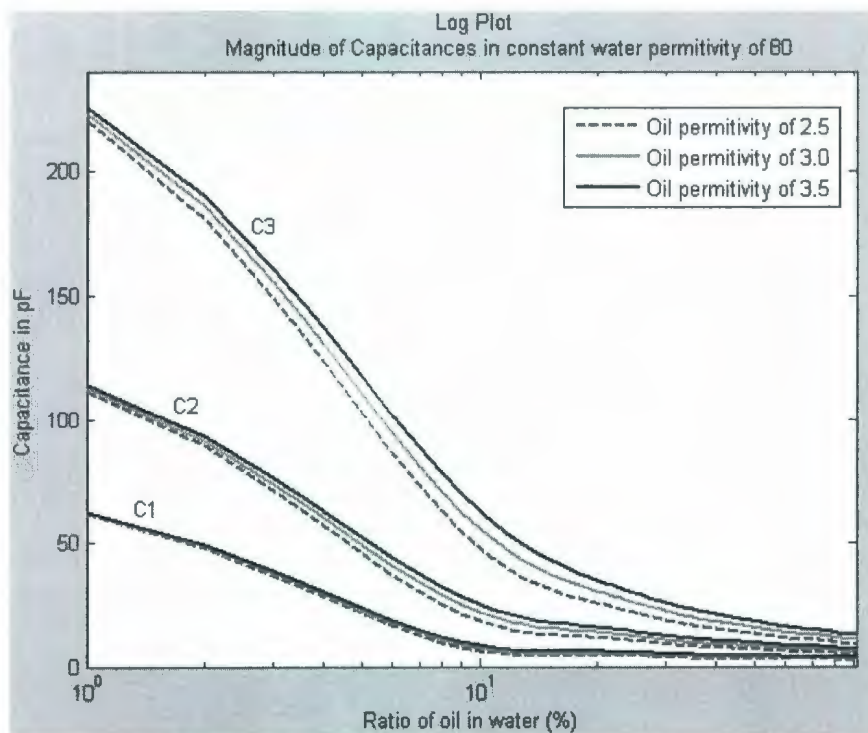


Figure 6.14: Inverse semi-log  $C = C(\alpha_w, \alpha_{oil}, \alpha_w = 80)$

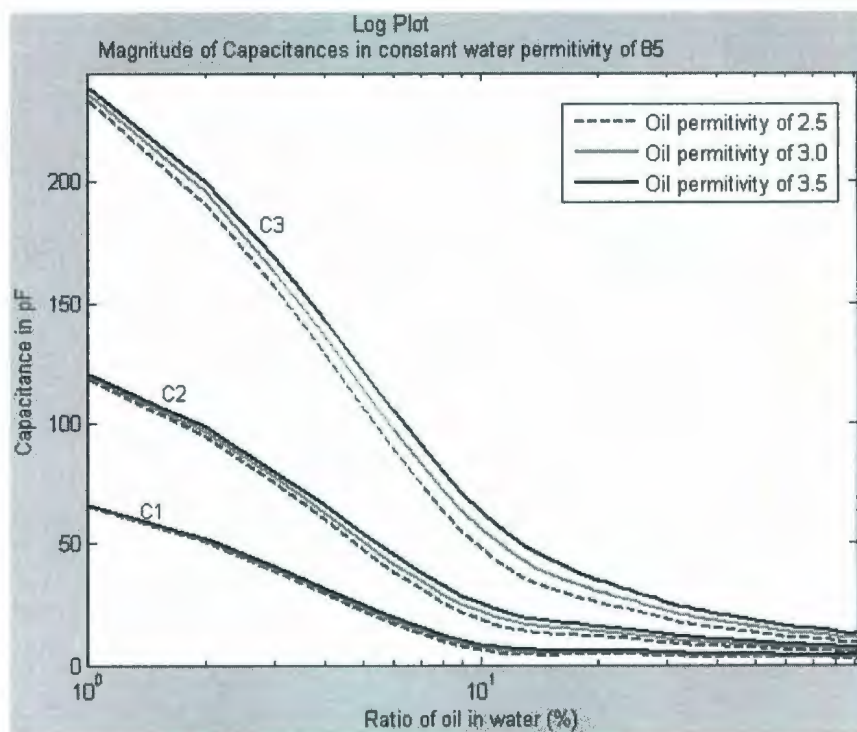


Figure 6.15: Inverse semi-log for  $C = C(\alpha_w, \alpha_{oil}, \alpha_w = 85)$

## Chapter 7

### Data Processing using Artificial Neural Network (ANN)

The concept of Artificial Neural Network (ANN) is widely used in applications of pattern recognition such as optical character reading, hand writing recognition, machine vision etc. The ANN has the ability to, remember many similar patterns and synthetic or classify them into categories or levels. ANN's proved useful also in applications where a mathematical model is very complex or unavailable.

Artificial neural network can establish an approximate model by fitting the relationship between given input/output data without requiring any fundamental physical theories.

In our case, despite of the assumption for stratified flow, small variations of the actual flow regimes are expected. For example, the stratifier can not break down possible emulsions. Also, it is quite difficult to extract the flow composition, and the material permitivities analytically from the measurement of capacitance. For these reasons, Artificial Neural Network was selected as primary data processing mechanism.

## 7.1 ANN Background

Artificial neural network (ANNs) are assemblies of many simple process called element neurons with a large connectivity between them. A neuron is an information-processing unit that is fundamental to the operation of a neuron network. The block diagram of Fig. 7.1 shows the model of a neuron, which forms the basis for designing (artificial) neural networks. Signals are passed between neurons over connection links with an associated weight. Specifically, a signal  $x_j$  at the input of connecting links  $j$  connected to neuron  $k$  is multiplied by the weight  $w_{kj}$ . An extra input ( $x_0 = b_k$ ) is defined for the purpose of biasing the neuron.  $b_k$  is always set to be on ( $b_k = 1$ ), multiplied by a weight equal to minus the threshold value and added in with all the other inputs.

Each neuron applies an activation function (usually nonlinear) to its net input (sum of the weighted input signals) to determine its output signal. The output of each unit may be given to several units including it self.

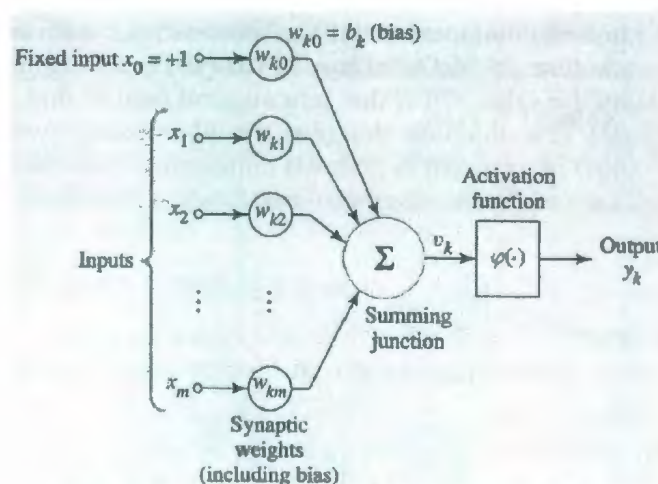


Fig. 7.1: Nonlinear model of neuron [54].



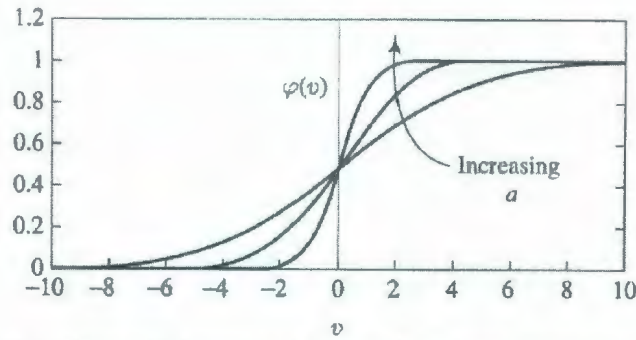


Fig.7.2: Sigmoid function for varying slope parameter  $a$  [54].

The amount of the output of one unit received by another unit depends on the strength of the connection between the units and the reflected in the weight value associated with the connecting link. This method of determining the weights on the connections is called learning or training. Given a required number of input and output sets, the network can be trained to identify the pattern.

The basic operation of an artificial neuron involves summing its weighted input signal and applying an output, or activation function, denoted by  $\varphi(v)$ .

The most common form of activation function used in the construction of artificial neural networks is sigmoid function (s-shaped curves). It is defined as strictly increasing function that exhibits a graceful balance between linear and nonlinear behavior. Different sigmoid functions can be used with different ranges. For example, a very popular function is the logistic sigmoid function with a range of  $[0, 1]$  given by

$$\varphi(v) = \frac{1}{1 + \exp(-av)} \quad (7.1)$$

where  $a$  is the slope parameter [55]. By varying the parameter  $a$ , we obtain sigmoid functions of different slopes, as illustrated in Fig. 7.2

The most widely used neural network is the Feedforward Multi-layer Perceptrons (MLP) network that distinguishes itself by the presence of one or more hidden layers, whose computation nodes are correspondingly called hidden neurons or hidden units.

The architectural graph in Fig. 7.3 illustrates the layout of a feedforward multilayer Perceptrons. In a fully connected net, each neuron in the input layer is connected to all the neurons in the first hidden layers, and each neuron in the hidden layer is connected either to all the neurons in the next hidden layer or to all the neurons in the output layer, with no interlayer connections. After verifying the network's structure, there is a need to determine the coefficient weights. By far the most popular method employed for weight training in MLP neural network is called Back Propagation solves the problem of missing information to the hidden layers, i.e. neither the input to nor the reference signals for the hidden layers are known, by taking the inputs to the hidden layers as being the inputs to the first layers propagated through the network. The reference signals for the hidden layers are then obtained by error back propagation through the network. Therefore, the synaptic weights are adjusted so as to make the actual response of the network move closer to desired response.

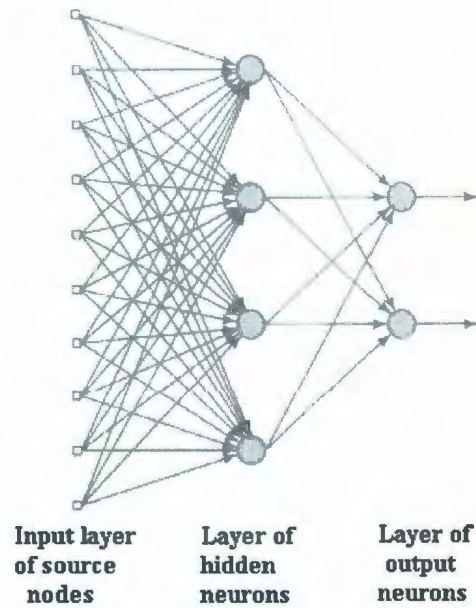


Fig. 7.3: Fully connected feedforward network with hidden layer and output layer [54]

## 7.2 Implementation and Results

### 7.2.1 Data collection

The flow measurement sensor consisting three electrode pairs have been simulated by finite element method (FEM), to generate the capacitance data set for training.

The data is collected based on FEM capacitance measurements of different variables parameters placed in three different representative locations within the conical sensor.

The three different variables parameters of water permittivities ( $\epsilon_{water} = 75, 80, 85$ ), oil permittivity of ( $\epsilon_{oil} = 2.5, 3.0, 3.5$ ) and percentage of oil in water (0:10:100%) were simulated. As a result, the data set was composed of 279 cases ( 99 values for each of the

capacitances) cases and 243 cases for linearization part, as indicated in previous part to linear the ranges of (10~90%).

The of ratio of oil in the flow is varied only between 10% to 100% in 10% increments to avoid large size neural network needed otherwise for mapping the highly non linear part of the characteristic in chapter 6 data plot.

The simulated results were arranged in input columns and output columns as given in Table 7.1.

### 7.2.2 Pre-processing of data

The main effort in artificial neural network development goes into collecting data and preprocessing them appropriately. Better performance is yield when the input values are normalized between -1 and 1 or 0 and 1. Therefore, with MATLAB commands the raw data were adopted for normalization before using it in the neural network model to generate input values internal between -1 and 1. The formula used in MATLAB command is (2)

$$\text{Normalized Value} = \frac{\text{Actual Value} - \text{Min Value}}{\text{Max Value} - \text{Min Value}} \quad (7.2)$$



In this application we use the three capacitances ( $C_1, C_2, C_3$ ) as inputs while  $\alpha, \varepsilon_0, \varepsilon_w$  are three outputs.

### 7.2.3 Implementation of neural network in MATLAB

For each neural network, different number of hidden layers and neurons were implemented using MATLAB Neural Network Toolbox [56].

In the implementation of a Back-Propagation multi-layer feedforward network (BPFN), determination of the optimal number for the hidden neurons is a crucial issue. If it is too small, the network can not take sufficient information and yields inaccurate approximating results. However, if this number be too big, the training will be very long.

In our application, through trial error experimentally proved fact, the numbers of neurons in each hidden layers are 6, 8, 9, 12, 15 and 16; however number of one and two hidden layers were selected for this network.

The weights were initialized to set weights and biases to new initial values. After the network weights were initialized, the network was trained. In MATLAB Toolbox, there are fourteen back-propagation training algorithms provided that all use the gradient of the performance function to determine how to adjust the weights to minimize performance. However, the fastest training algorithm for the network of moderate size, Levenberg-Marquardt algorithm (TRAINLM), was used because of memory reduction feature for use when training set is large. The performance function used for BPFN was mean square error (mse), the average square error between the network outputs and the target outputs.

Also, for each, the networks were trained for 5500 epochs where an epoch consists of one sweep through the entire training data.

## 7.2.4 Results and Discussion

We tested fourteen different neural networks with different network configurations. We have found out that the number of 7 and 9 neurons in the two hidden layers resulted in the most compact and efficient performance. The network configuration is shown in Figure 7.4.

The first network configuration we tested had found 9 neurons in the hidden layers as shown in Figure 7.4

Error curve in Fig. 7.5 show we reached the converging after 3500 epochs while the final error was approximately 0.03.

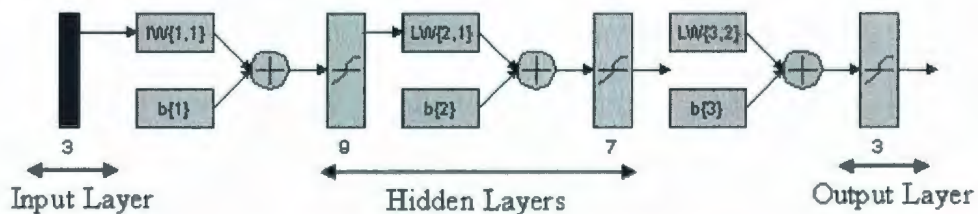


Figure 7.4: Schematic of the designed network with two hidden layers; layer one with 9 neurons and the layer two with 7 neurons.

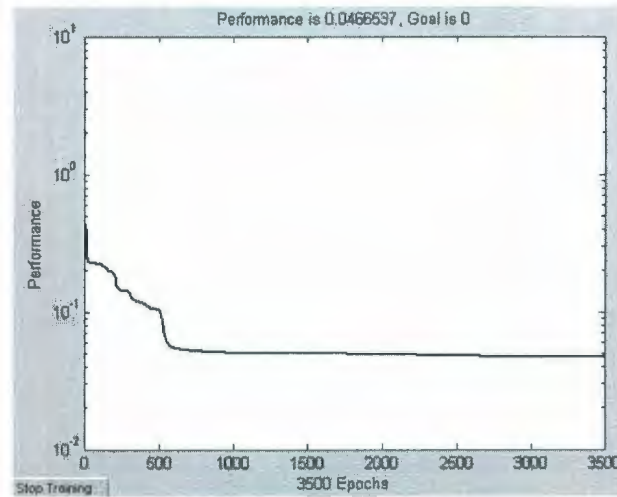


Fig. 7.5: Training performance with epochs of 3500

Next we tested a neural network with one hidden layer having 4, 7, 10, 13, 15 and 16 neurons in sequence. The configuration of the network is shown in Figure 7.6, for this network for instance the number of neuron in the hidden layer is 15.

The 15 neuron hidden layer network had the error in the region of  $10^{-7}$  while also exhibiting rather fast learning curve, shown in Figure 7.6.

Also the de-normalized values of the ANN output is shown in the last three columns of Table 7.1

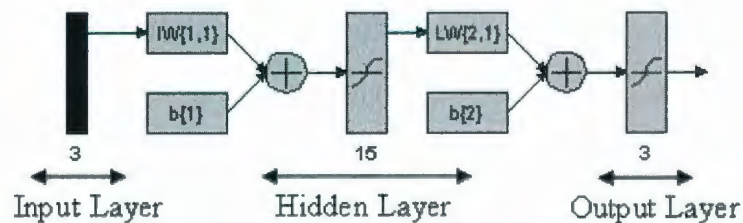


Figure 7.6: Schematic of the designed network of one layer with 10 neurons.

## 7.3 Concluding Remarks

We applied a data processing method based on using an Artificial Neural Network to deal with possible measurement uncertainties. In practice each sensor device undergoes an initial calibration in which the ANN is trained on some representative data. We have found that ANN having one hidden layer of 15 neurons is capable of mapping capacitance data input into three outputs, the phase ratio, and phase permittivities with a very small error.

It is our future plan described in the following chapter, to test this data processing on real measurement data.



Table 7.1: The final simulated results

INPUT			OUTPUT(ANSYS)			OUTPUT(Simulated, nntool)		
C1	C2	C3	$\mathcal{E}_{water}$	$\mathcal{E}_{oil}$	$\times(\%(10))$	$\mathcal{E}_{water}$	$\mathcal{E}_{oil}$	$\%(10)$
2.46	4.365	8.368	75	2.5	0			
2.957	5.238	10.041	75	3	0			
3.45	6.111	11.715	75	3.5	0			
2.46	4.365	8.368	80	2.5	0			
2.957	5.238	10.041	80	3	0			
3.45	6.111	11.715	80	3.5	0			
2.46	4.365	8.368	85	2.5	0			
2.957	5.238	10.041	85	3	0			
3.45	6.111	11.715	85	3.5	0			
2.543	4.995	9.092	75	2.5	1.00	75.0000	2.5000	1.0000
3.0513	5.965	10.904	75	3	1.00	75.0000	2.9998	1.0000
3.5592	6.9285	12.715	75	3.5	1.00	75.0000	3.5000	1.0000
2.5431	5.003	9.0935	80	2.5	1.00	80.0000	2.5000	1.0000
3.0515	5.9761	10.906	80	3	1.00	80.0000	3.0000	1.0000
3.5594	6.941	12.718	80	3.5	1.00	80.0000	3.5000	1.0000
2.5435	5.003	9.094	85	2.5	1.00	84.9973	2.5000	1.0000
3.0517	5.986	10.908	85	3	1.00	85.0000	3.0001	1.0000
3.5598	6.953	12.720	85	3.5	1.00	85.0000	3.5000	1.0000
2.6456	5.27	9.687	75	2.5	2.00	75.0000	2.5000	2.0032
3.1734	6.298	11.612	75	3	2.00	75.0000	2.9999	1.9963
3.700	7.318	13.533	75	3.5	2.00	75.0000	3.5000	2.0020

2.6459	5.278	9.69	80	2.5	2.00	80.0000	2.5000	1.9966
3.1738	6.3079	11.617	80	3	2.00	80.0000	3.0000	2.0040
3.7014	7.330	13.54	80	3.5	2.00	80.0000	3.5000	1.9977
2.6462	5.284	9.693	85	2.5	2.00	84.9985	2.5000	1.9983
3.1743	6.316	11.621	85	3	2.00	85.0000	3.0001	2.0038
3.702	7.342	13.545	85	3.5	2.00	85.0000	3.5000	1.9982
2.7000	5.629	10.486	75	2.5	3.00	75.0000	2.5000	3.0024
3.237	6.727	12.560	75	3	3.00	75.0000	2.9998	3.0039
3.7748	7.816	14.627	75	3.5	3.00	75.0000	3.5000	2.9955
2.7005	5.637	10.492	80	2.5	3.00	80.0000	2.5000	2.9995
3.238	6.7379	12.569	80	3	3.00	80.0000	3.0000	2.9995
3.776	7.830	14.639	80	3.5	3.00	80.0000	3.5000	3.0009
2.7010	5.644	10.497	85	2.5	3.00	85.0000	2.5000	2.9997
3.239	6.747	12.576	85	3	3.00	85.0000	3.0001	2.9935
3.777	7.842	14.649	85	3.5	3.00	85.0000	3.5000	3.0051
2.803	6.08	11.442	75	2.5	4.00	75.0000	2.5000	4.0044
3.360	7.262	13.693	75	3	4.00	75.0000	3.0002	4.0007
3.915	8.45	15.933	75	3.5	4.00	75.0000	3.5000	3.9994
2.8035	6.089	11.452	80	2.5	4.00	80.0000	2.5000	3.9984
3.361	7.275	13.707	80	3	4.00	80.0000	3.0001	4.0006
3.917	8.451	15.951	80	3.5	4.00	80.0000	3.4999	4.0001
2.804	6.096	11.461	85	2.5	4.00	85.0000	2.5000	3.9969
3.3625	7.286	13.72	85	3	4.00	85.0000	2.9997	3.9989
3.919	8.466	15.968	85	3.5	4.00	85.0000	3.4999	4.0004
2.976	6.65	12.888	75	2.5	5.00	75.0000	2.5000	5.0000
3.569	7.938	15.403	75	3	5.00	75.0000	3.0000	4.9981
4.157	9.212	17.898	75	3.5	5.00	75.0000	3.4999	5.0043



2.966	6.662	12.905	80	2.5	5.00	80.0000	2.5000	5.0014
3.571	7.954	15.427	80	3	5.00	80.0000	2.9999	5.0001
4.16	9.233	17.938	80	3.5	5.00	80.0000	3.4999	4.9936
2.968	6.672	12.919	85	2.5	5.00	85.0000	2.5000	4.9988
3.573	7.968	15.448	85	3	5.00	85.0000	3.0000	5.0024
4.1627	9.252	17.958	85	3.5	5.00	84.9995	3.4999	5.0018
3.198	7.543	15.104	75	2.5	6.00	75.0000	2.5000	5.9961
3.828	8.989	18.015	75	3	6.00	75.0000	3.0000	6.0008
4.456	10.417	20.891	75	3.5	6.00	75.0000	3.5000	6.0000
3.2	7.559	15.132	80	2.5	6.00	80.0000	2.5000	6.0003
3.8325	9.0128	18.056	80	3	6.00	80.0000	3.0000	5.9959
4.461	10.447	20.946	80	3.5	6.00	80.0000	3.5000	5.9989
3.202	7.574	15.158	85	2.5	6.00	85.0000	2.5000	6.0031
3.835	9.0334	18.092	85	3	6.00	85.0000	3.0000	6.0032
4.465	10.475	20.995	85	3.5	6.00	85.0000	3.5000	6.0011
3.581	8.87	18.522	75	2.5	7.00	75.0000	2.5000	6.9992
4.281	10.547	22.023	75	3	7.00	75.0000	3.0000	6.9997
4.977	12.194	25.462	75	3.5	7.00	75.0000	3.5000	7.0005
3.585	8.8966	18.576	80	2.5	7.00	80.0000	2.5000	7.0008
4.287	10.583	22.108	80	3	7.00	80.0000	3.0000	7.0006
4.985	12.242	25.563	80	3.5	7.00	80.0000	3.5000	7.0001
3.588	8.919	18.623	85	2.5	7.00	85.0000	2.5000	7.0001
4.292	10.615	22.1669	85	3	7.00	85.0000	3.0000	6.9999
4.992	12.285	25.653	85	3.5	7.00	85.0000	3.5000	6.9995
4.254	11.553	25.229	75	2.5	8.00	75.0000	2.5000	7.9996
5.075	13.672	30.2	75	3	8.00	75.0000	3.0001	7.9989
5.887	15.733	34.702	75	3.5	8.00	75.0000	3.5000	8.0000

4.261	11.604	25.684	80	2.5	8.00	80.0000	2.5000	8.0005
5.086	13.743	30.375	80	3	8.00	80.0000	3.0000	8.0008
5.902	15.827	34.932	80	3.5	8.00	80.0000	3.5000	8.0000
4.268	11.65	25.796	85	2.5	8.00	85.0000	2.5000	7.9999
5.096	13.807	30.531	85	3	8.00	85.0000	3.0000	8.0002
5.915	15.911	35.139	85	3.5	8.00	84.9997	3.5000	8.0000
6.158	18.098	47.209	75	2.5	9.00	75.0000	2.5000	8.9999
7.304	21.643	54.75	75	3	9.00	75.0000	3.0001	9.0000
8.424	25.000	61.806	75	3.5	9.00	75.0000	3.5000	9.0000
6.181	18.324	47.728	80	2.5	9.00	80.0000	2.5000	8.9999
7.336	21.880	55.477	80	3	9.00	80.0000	3.0000	9.0000
8.466	25.018	62.694	80	3.5	9.00	80.0000	3.5000	9.0000
6.201	18.697	48.195	85	2.5	9.00	85.0000	2.5000	8.9999
7.364	21.998	56.078	85	3	9.00	84.9999	3.0000	9.0000
8.504	25.265	63.5	85	3.5	9.00	84.9997	3.5000	9.0000
73.931	130.96	251.044	75	2.5	10.00			
73.931	130.96	251.044	75	3	10.00			
73.931	130.96	251.044	75	3.5	10.00			
78.86	139.69	267.78	80	2.5	10.00			
78.86	139.690	267.78	80	3	10.00			
78.86	139.690	267.78	80	3.5	10.00			
83.789	148.421	284.516	85	2.5	10.00			
83.789	148.421	284.516	85	3	10.00			
83.789	148.421	284.516	85	3.5	10.00			



## Chapter 8

### Conclusion and Future Work

The research presented in this thesis is focused on the design and simulation of a capacitance-based component ratio measuring instrument applied to multiphase flows.

The research presented in this thesis is focused on design and simulation of a capacitance-based component ratio measuring instrument applied to multiphase flows.

Many commercial devices are available today; however, our sensor exceeds these by being able to measure the flow composition under drifting of phase properties, namely the permittivities. This is performed by constructing an array of linearly-independent measurements that can uniquely resolve the desired composition plus the material properties.

Our sensor also outperforms the designs that use mixers or homogenizers by introducing a conical hydrocyclone as phase stratifier. In this non-mixing process, we do not create emulsions that may become hard to break down mechanically using harsh chemicals.

This research work has been conducted at the theoretical level only but is prepared for practical evaluation in the near future. So far, we have built a bench-top multiphase loop

depicted in Figure 8.1 and fabricated the sensor components that currently undergo an assembly.

Because the capacitances were not obtained in a closed form but rather calculated using an idealized model that was processed by FEM, it is unlikely that any practical implementation would follow closely these conditions. There are other factors that influence the concentration reading, such as total volumetric flow, emulsion phases, etc. The FEM evaluation was also conducted only at a coarse sampling region, therefore, using an ANN for signal processing seems appropriate, especially in view of future expansions into detection of three phase flows. Other techniques, such as curve fitting and polynomial regression, will be tested on real data set in future.

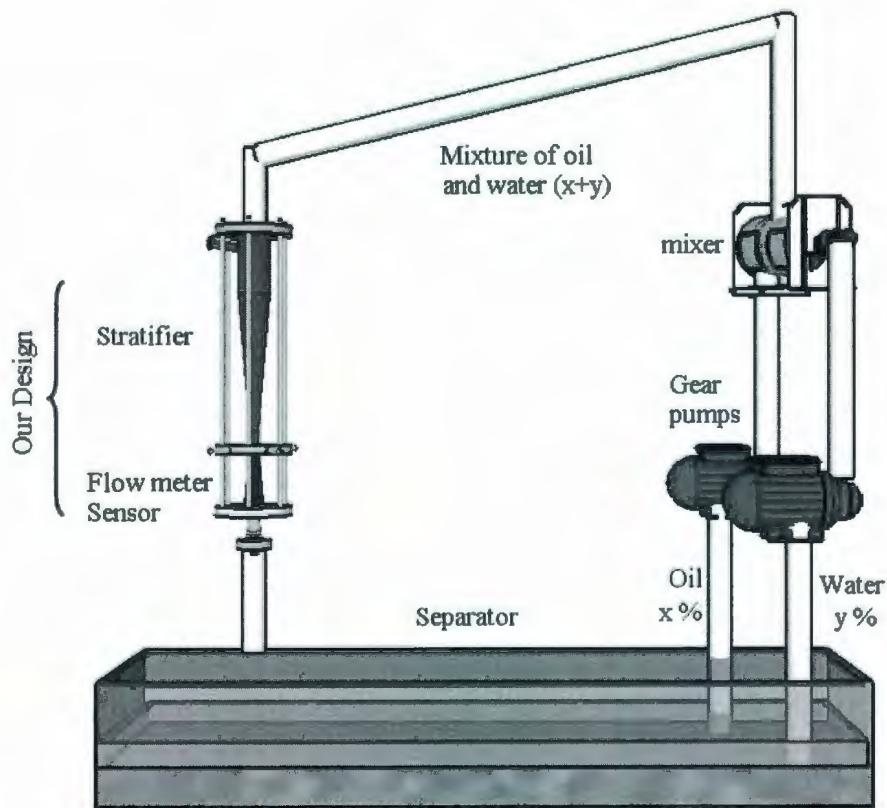


Figure 8.1: Control Loop: Two-phase Separator and Flow-sensor Evaluator

# APPENDIX

## Matlab Program Code:

```
%%%% C1: Data for capacitance values of C1 %%%%%%%%%%%%%%%
% a=[10 20 30 40 50 60 70 80 90];
%
C12575=[2.5430 2.6456 2.7000 2.803 2.976 3.198 3.581 4.254
6.158];
C13075=[3.0513 3.1734 3.237 3.360 3.569 3.828 4.281 5.075 7.304];
C13575=[3.5592 3.700 3.7748 3.915 4.157 4.456 4.977 5.887 8.424];
C12580=[2.5431 2.6459 2.7005 2.8035 2.966 3.200 3.585 4.261
6.181];
C13080=[3.0515 3.1738 3.238 3.361 3.571 3.8325 4.287 5.086 7.336];
C13580=[3.5594 3.7014 3.776 3.917 4.16 4.461 4.985 5.902 8.466] ;
C12585=[2.5435 2.6462 2.7010 2.804 2.968 3.202 3.588 4.268 6.201];
C13085=[3.0517 3.1743 3.239 3.3625 3.573 3.835 4.292 5.096 7.364];
C13585=[3.5598 3.702 3.777 3.919 4.1627 4.465 4.992 5.915 8.504];
%%%% C2: Data for capacitance values of C2 %%%%%%%%%%%%%%%
%
C22575=[4.995 5.270 5.629 6.08 6.65 7.543 8.870 11.553 18.098];
C23075=[5.965 6.298 6.727 7.262 7.938 8.989 10.547 13.672 21.643];
C23575=[6.9285 7.318 7.816 8.45 9.212 10.417 12.194 15.733
25.000];
C22580=[5.003 5.278 5.637 6.089 6.662 7.559 8.8966 11.604 18.324];
C23080=[5.9761 6.3079 6.7379 7.275 7.954 9.0128 10.583 13.743
21.880];
C23580=[6.941 7.330 7.830 8.451 9.233 10.447 12.242 15.827
25.018];
C22585=[5.003 5.284 5.644 6.096 6.672 7.574 8.919 11.650 18.697];
C23085=[5.986 6.316 6.747 7.286 7.968 9.0334 10.615 13.807
21.998];
C23585=[6.953 7.342 7.842 8.466 9.252 10.475 12.285 15.911 25.26];
%
%%%% C3: Data for capacitance values of C3 %%%%%%%%%%%%%%%
%
C32575=[9.092 9.687 10.486 11.442 12.888 15.104 18.522 25.229
47.209];
C33075=[10.904 11.612 12.560 13.693 15.403 18.015 22.023 30.2
54.75];
C33575=[12.715 13.533 14.627 15.933 17.898 20.891 25.462 34.702
61.806];
C32580=[9.0935 9.690 10.492 11.452 12.905 15.132 18.576 25.684
47.728];
C33080=[10.906 11.617 12.569 13.707 15.427 18.056 22.108 30.375
55.477];
C33580=[12.718 13.54 14.639 15.951 17.938 20.946 25.563 34.932
62.694];
C32585=[9.094 9.693 10.497 11.461 12.919 15.158 18.623 25.796
48.195];
C33085=[10.908 11.621 12.576 13.720 15.448 18.092 22.1669 30.531
6.078];
C33585=[12.720 13.545 14.649 15.968 17.958 20.995 25.653 35.139
63.5];
```



```
%%%%%%%% Creating the format of table for inputting the neural network
```

```
C_1=[C12575' C13075' C13575' C12580' C13080' C13580' C12585' C13085'  
C13585'];  
C_2=[C22575' C23075' C23575' C22580' C23080' C23580' C22585' C23085'  
C23585'];  
C_3=[C32575' C33075' C33575' C32580' C33080' C33580' C32585' C33085'  
C33585'];
```

```
C1=[];  
C2=[];  
C3=[];  
Op=[];  
for i=1:9  
    C1=[C1 ;C_1(i,:)'];  
    C2=[C2 ;C_2(i,:)'];  
    C3=[C3 ;C_3(i,:)'];  
end  
for i=2:10  
    Op=[Op ;[i-1; i-1; i-1; i-1; i-1; i-1 ;i-1; i-1; i-1]];  
end
```

```
%%%%%%%% Normalization  
Oo=repmat([2.5; 3; 3.5],[27,1]);  
Ow=repmat([75;75;75;80;80;80;85;85;85],[9,1]);
```

```
I=[C1';C2';C3'];  
O=[Ow';Oo';Op'];
```

```
[I1,PS_i] = mapminmax(I);  
[O1,PS_o] = mapminmax(O);
```

A For de normalization:

```
%%%%%%%% o_sim1=mapminmax('reverse',k_1,PS_o)
```

PLOTTING

```
o_sim1=mapminmax('reverse',e_r,PS_o)';
```

```
%subplot(2,1,1);  
figure(1)  
plot(O(2:3,:))';  
hold on  
plot(o_sim1(:,2:3))
```

```
%subplot(2,1,2);  
figure(2)  
plot(O(1,:))';  
hold on  
plot(o_sim1(:,1))
```

```

network1 = Neural Network object:

architecture:      numInputs: 1
                   numLayers: 2
                   biasConnect: [1; 1]
                   inputConnect: [1; 0]
                   layerConnect: [0 0; 1 0]
                   outputConnect: [0 1]
                   targetConnect: [0 1]

                   numOutputs: 1 (read-only)
                   numTargets: 1 (read-only)
                   numInputDelays: 0 (read-only)
                   numLayerDelays: 0 (read-only)

subobject structures:
                   inputs: {1x1 cell} of inputs
                   layers: {2x1 cell} of layers
                   outputs: {1x2 cell} containing 1 output
                   targets: {1x2 cell} containing 1 target
                   biases: {2x1 cell} containing 2 biases
                   inputWeights: {2x1 cell} containing 1 input weight
                   layerWeights: {2x2 cell} containing 1 layer weight

functions:
                   adaptFcn: 'trains'
                   gradientFcn: 'calcjx'
                   initFcn: 'initlay'
                   performFcn: 'mse'
                   trainFcn: 'trainlm'

parameters:
                   adaptParam: .passes
                   gradientParam: (none)
                   initParam: (none)
                   performParam: (none)
                   trainParam: .epochs, .goal, .max_fail, .mem_reduc,
                               .min_grad, .mu, .mu_dec, .mu_inc,
                               .mu_max, .show, .time

weight and bias values:
                   IW: {2x1 cell} containing 1 input weight matrix
                   LW: {2x2 cell} containing 1 layer weight matrix
                   b: {2x1 cell} containing 2 bias vectors

other:
                   userdata: (user information)

```

*Chart 7.1: Architecture and properties of designed network configuration*

# Bibliography

- [1] "Void fraction measurements in gas-liquid flows using capacitance sensors"; Kenneth J. Elkow and Kamiel S Rezkallah , Meas. Sci. Technol. 7 (1996) 1153-1163.
- [2] S. Corneliussen, J. P. Couput, E. Dahl, E. Dykesteen, K. E. Frøysa, E. Malde, H. Moestue, P. O. Moksnes, L. Scheers, and H. Tunheim, "Handbook of multiphase flow metering", Mar. 2005.
- [3] E. Dykesteen, A. Hallanger, E. Hammer, E. Samnøy, and R. Thorn, "Non-intrusive three-component ratio measurement using an impedance sensor", Journal of Physics E: Scientific Instruments, vol. 18, no. 5, pp. 540-544, June 1985.
- [4] "Capacitive sensors: design and applications". L. K. Baxter, New York: IEEE Press, 1997.
- [5] "A capacitance sensor for two-phase void fraction measurement and flow pattern identification", J.J.M. Gerate and J.C. Borast, Int. J. Multiphase flow Vol. 14, No. 3, 1988
- [6] Richard Thorn, Geir Anton Johansen, Erling A Hammer , "recent developments in three-phase flow measurement", 1st World Congress on Industrial Process Tomography, Buxton, Greater Manchester, April 14-17, 1999.
- [7] "Capacitance Sensors for Measurement of Phase Volume Fraction in Two-Phase Pipelines", Cristina N. Strizzolo and JosC Converti; IEEE Transactions on instrumentation and measurement, VOL. 42, NO. 3, June 1993
- [8] "Framo multiphase flowmeters phasewatcher vx," Jan. 2006. [Online]. Available: <http://www.framoeng.no/Files/Bulletins/FramoMultiphaseFlowMeters2003.pdf>
- [9] R. Thorn, G. A. Johansen, and E. A. Hammer, "Recent developments in three-phase flow measurement," Meas. Sci Technol., vol. 8, no. 7, pp. 691-701, 1997.
- [10] T. S. Whitaker, "Multiphase flow measurement: current and future developments [for offshore industry use]," in Advances in Sensors for Fluid Flow Measurement, IEE Colloquium on, Apr. 18, 1996, pp. 101-111.
- [11] "Non-Invasive two phase flow measurement using soft X-ray attenuation", J. Menuell, B Byrne, Y Yan (University of Teesside, UK)
- [12] "Design of capacitance sensor system for void fraction measurement", LIU Yi-ping, NIU Gang, WANG Jing; Journal of Zhejiang University Science.



- [13] "Capacitance Sensors for Void-Fraction Measurements and Flow-Pattern Identification in Air–Oil Two-Phase Flow", Wael H. Ahmed, IEEE Sensors journal, Vol. 6, NO. 5, October 2006 1153
- [14] "A capacitance sensor for the characterization of microgravity two-phase liquid–gas flows", Devin Lowe and Kamel S Rezkallah, Meas. Sci. Technol. 10 (1999) 965–975. Printed in the UK
- [15] "Measurement of void fraction in vertical gas-liquid two-phase flow by ring type capacitance transducers", J.S. Chang, R. Girard, R. Raman, and F.B.P. Tran, department of engineering physics, McMaster university.
- [16] "The Use of a Coaxial Capacitor as a Capacitance Sensor for Phase Percentage Determination in Multiphase Pipelines", Salah I. Al-Mously, Member, IEEE, and Ahmed Y. Ahmed
- [17] "An Online Flow Pattern Identification System for Gas–Oil Two-Phase Flow Using Electrical Capacitance Tomography", Dailiang Xie, Zhiyao Huang, Haifeng Ji, and Haiqing Li, IEEE Transactions on instrumentation and measurement, Vol. 55, No. 5, October 2006
- [18] "Modeling of capacitance tomography sensors", W.Q. Yang, IEE Proc.-Sci. Meas. Technol., Vol. 144, No. 5, September 1997
- [19] "Application of Electrical Capacitance Tomography to the Void Fraction Measurement of Two-Phase Flow", Zhiyao Huang, Baoliang Wang, and Haiqing Li, IEEE Transactions on instrumentation and measurement, Vol. 52, No. 1, February 2003
- [20] "Development of capacitance tomographic imaging systems for oil pipeline measurements", W.Q. Yang, A. L. Stott, and M. S. Beck, Rev. Sci. Instrum. 66(8), August 1995
- [21] "Electrical Capacitance Tomography—Sensor Models, Design, Simulations, and Experimental Verification", Kjell Joar Alme and Saba Mylvaganam, IEEE Sensors Journal, Vol. 6, No. 5, October 2006
- [22] "Detection of oil in water and water in oil emulsions inside a phase separator washing tank", university of Magallanes, Chile.
- [23] A Computational Study of Particle Separation in Hydrocyclones; E. Statie, M. Salcudean, I. Gartshore and E. Bibeau; Journal of Pulp and Paper Science
- [24] A Simple procedure for design and performance prediction of Bradley and Rietema hydrocyclone, R. Castilho and R.A. Medronho



- [25] "Oil/water separation in liquid/liquid hydrocyclones", Part 1-experimental investigation, Carlos Gomez, Juan Caldentey, and Shoubo Wang, SPE.
- [26] "Application of the liquid cyclone in biological separation", Enrique Ortega-Rivas, Eng. Life Sci. 2004, No.2
- [27] A new method for yeast recovery in batch ethanol fermentations: Filter aid filtration followed by separation of yeast from filter aid using hydrocyclones Virginia Martins da Mattal & Ricardo de Andrade Medronho2.
- [28] A model for performance prediction of hydrocyclones ,M.A.Z. Coelho a, R.A. Medronhob.
- [29] A Computational Study of Particle Separation in Hydrocyclones, E. Statie, M. Salcudean, I. Gartshore and E. Bibeau
- [30] "Preliminary results of large eddy simulations of a hydrocyclone", F. J. Souzaa, and A. Silveira Netob, Engenharia Térmica (Thermal Engineering), Vol. 3 · No. 2 · December 2004 · p. 168-173
- [31] Deoiling Hydrocyclones, Syed K. Ah and Charles A. Petty, Department of Chemical Engineering Michigan State University, East Lansing, MI 48824
- [32] A model for performance prediction of hydrocyclones, M.A.Z. Coelho a, R.A. Medronhob,
- [33] K. Nishigaki, M. Takeda, N. Tomomori, and A. Iwata, "Basic study on oil separation from oil-contaminated seawater by MHD method" (in Japanese), Teionkougaku, vol. 37, no. 7, pp. 343–349, 2001.
- [34] "Flow Control of Seawater with a Diverging Duct by MHD Separation Method"; Minoru Takeda, Naotaka Tomomori, Teruhiko Akazawa, Kazu Nishigaki, and Akira Iwata; IEEE Transactions on applied superconductivity, VOL. 14, NO. 2, JUNE 2004.
- [35] "Methods for Improving Hydrocyclone Design "; A. M. Kutepov, M. G. Lagutkin, I. G. Ternovskii and L. G. Tsyganov; 1992 Plenum Publishing Corporation
- [36] T. S. Whitaker, "Multiphase flow measurement: current and future developments for offshore industry use], in Advances in Sensors for Fluid Flow Measurement, IEEE Colloquium on, Apr. 18, 1996, pp. 101-111.
- [37] "Design of a DSP-Based Impedance Measuring Instrument for Multiphase flowmeter" Master thesis: Xiang Fang, Memorial University, St. John's, Canada
- [38]"Electromagnetic field theory fundamentals", Curu Hiziroclu, Cambridge University Press; 2 edition (22 Jul 2004)

- [39] "Concept of Electric and Magnetic field", Mohhamad Gavami, University of Tehran, Iran, 2nd Edition
- [40] "Analog Devices, Linear Output Magnetic Field Sensor", AD22151, datasheet.
- [41] "Electromagnetic visualization technique for non-metallic inclusions in a melt", Sergey Makarov, Reinold Ludwing and Diran Apelian.
- [42] "Electromagnetic Separation Techniques in Metal Casting" I. Conventional Methods Sergey Makarov, Member, IEEE, Reinhold Ludwig, Senior Member, IEEE, and Diran Apelian.
- [43] R. L. Sergey Makarov and D. Apelian, "Electromagnetic visualization technique for non-metallic inclusions in a melt," Means. Sci.Technol, vol. 10, July 1999.
- [44] "Flow Control of Seawater with a Diverging Duct by MHD Separation Method", Minoru Takeda, Naotaka Tomomori, Teruhiko Akazawa, Kazu Nishigaki, and Akira Iwata, IEEE Transactions on Applied Superconductivity, VOL. 14, NO. 2, JUNE 2004
- [45] "Fundamentals of Electromagnetics with MATLAB", Second Edition by Karl E. Lonngren, SciTech Publishing, Inc.,
- [46] "Velocity-Profile Deviations Influence Flowmeter Performance", By Corte Swearingen Reprinted from Chemical Processing magazine
- [47] Fundamental Studies of Helical-Type Seawater MHD Generation System Minoru Takeda, Yasuaki Okuji, Teruhiko Akazawa, Xiaojun Liu, and Tsukasa Kiyoshi, IEEE TRANSACTIONS ON APPLIED SUPERCONDUCTIVITY, VOL. 15, NO. 2, JUNE 2005
- [48] Rhodes, N., Pericleous, K., and Drake, S.: "The Prediction of Hydrocyclone Performance with a Mathematical Model," Proc., 1987 International Conference on Hydrocyclones, Oxford, England, 51-58 (1987)
- [49] "Optimum form of capacitive transducer for displacement measurement"; Masahide Himawa Mitsunobo Nakamm and Makoto Kanno, , IEEE Transaction on Instrumentation Measurement, Vol. IM-33, no. 4. pp. 276-280, December 1984.
- [50] "Capacitance change indicates liquid Levels"; T. L Oreenwood, Ektronlcs, p. 67. Aug, 1960.
- [51] "Void fraction measurements in gas liquid flows using capacitance sensors" ;Elkow K J and Rezkallah K S 1996 ,Meas. Sci. Technol. 7 1153-63
- [52] ANSYS, version 5.4 software

- [53] "The Finite Element Method in Electromagnetics"; by Jianming Jin, 2nd edition
- [54] "Neural networks, a comprehensive foundation", Simon Haykin, Prentice Hall 1999
- [55] "Neural Networks for Control", Zalzala/Morris, Ellis Horwood 1996
- [56] MATLAB Neural Network Toolbox, version 2006







